[American Journal of Science, Vol. 321, November, 2021, P. 1350–1379, DOI 10.2475/09.2021.03]

NEOARCHEAN BASEMENT, MANTLE ENRICHMENT AND CRUSTAL EXTRACTION IN CENTRAL ASIA: PETROGENESIS OF 2.5 GA AMPHIBOLITE AND METADIORITE IN NE CHINA

HUICHUAN LIU*,**,†, JUN SHAO***, GUANGYOU ZHU§, and YINGLEI LI§§,§§§

ABSTRACT. Archean basement in the Central Asian Orogenic Belt (CAOB) is relatively rare, but it has the potential to provide additional information on the processes of lithospheric mantle enrichment and crust extraction processes during the early history of the Earth. We identified Neoarchean amphibolite (2537−2565 Ma) and metadiorite (2481−2539 Ma) in the Biliya area of the Erguna Terrane in the southeast CAOB. The amphibolite is geochemically MORB-like and has a weakly left-leaning REE pattern, and low zircon εHf(t) (−0.7− +6.2), and whole-rock εNd(t) (−1.7–+4.5) and εHf(t) (−1.9) values. Our petrogenetic modeling reveals that the amphibolite is derived from ~20 % partial melting of the lithospheric mantle in the spinel stability field (~65 km depth). The metadiorite shows near-zero εNd(t) (−0.5–+3.6) and εHf(t) (+0.5–+1.4) values and is likely derived from partial melting of mafic lower crust. The metadiorite and amphibolite likely formed in an extensional continental arc/back-arc setting and represent the Archean crystalline basement of the microcontinents within the CAOB. Three-staged mantle segregation and crust extraction processes have been proposed: (a) 20 % melt extraction from primitive mantle-like lithospheric mantle, leaving behind a depleted mantle; (b) subduction-related fluid/melt metasomatism of the lithospheric mantle and its partial melting, generating the arc-type enriched mantle and mafic lower crust; and (c) partial remelting of the mafic lower crust produced the Tonalite-trondhjemite-granodiorite (TTG) crust.

Key words: Lithospheric mantle, Crust extraction, Continental basement, Neoarchean Earth, Central Asian Orogenic Belt

INTRODUCTION

The Earth's lithospheric mantle shields the crust from the convecting asthenospheric mantle (Hofmann, 1988; van Hunen and Moyen, 2012). After four billion years of complex depletion and enrichment events, the present mantle is geochemically heterogeneous and dominated by four isotopic endmembers, namely the depleted mantle (DM), enriched mantle type I (EM I), enriched mantle type II (EM II) and high μ mantle (HIMU; Zindler and others, 1982; Anderson, 1983; White, 1985; Salters and Stracke, 2004). Although the nature of these four mantle endmembers has been clarified through extensive isotope studies, features of the lithospheric mantle and its mantle depletion and enrichment processes are still unclear. Furthermore, how the volume of continental crust was extracted from the upper mantle throughout the Earth history (crustal growth) remains poorly understood (Hawkesworth and Kemp, 2006; Kemp and others, 2009; Hawkesworth and others, 2010; Cawood and others, 2013; Cawood and Hawkesworth, 2019). The Archean is a

* State Key Laboratory of Petroleum Resources and Prospecting, China University of Petroleum (Beijing), Beijing 102249, China
** College of Geosciences, China University of Petroleum (Beijing), Beijing 102249, China
*** Shenyang Institute of Geology and Mineral Resources/Shenyang Center of Geological Survey, China Geological Survey, Shenyang 110034, China
§ Research Institute of Petroleum Exploration and Development, PetroChina, Beijing 100083, China
§§ Key Laboratory of Orogen and Crust Evolution, Department of Geology, Peking University, Beijing 100871, China
§§§ Institute of Mineral Resources, Chinese Academy of Geological Sciences, Beijing 100037, China
† Corresponding author: Huichuan Liu (liuhuichuan1986@126.com)

key stage of the mantle depletion and crustal extraction, and Archean rocks are important records of early Earth lithospheric mantle and crust (Hawkesworth and Kemp, 2006; Hawkesworth and others, 2010; Cawood and others, 2013; Cawood and Hawkesworth 2019).

The Central Asian Orogenic Belt (CAOB), situated between the Siberia and Baltica cratons to the north and the North China and Tarim cratons to the south, encompasses an immense region from the Urals in the west to the Russian Far East and includes tens of microcontinents and subduction-accretionary complexes (fig. 1A; Wilde and Zhou, 2015; Xiao and others, 2015; Zhou and others, 2018). The CAOB is known as the world's largest area of Phanerozoic juvenile crust formation, and much attention has been paid to its Phanerozoic crustal growth (Tang and others, 2010; Kovach and others, 2013; Eizenhöfer and others, 2015). No robust evidence of Archean upper mantle and crystalline basement have been reported for these microcontinents within the CAOB. Recent high-precision detrital zircon dating has revealed that sedimentary rocks previously ascribed to the Precambrian have Paleozoic or even Mesozoic maximum depositional ages (Miao and others, 2007; Xie and others, 2008; Wu and others, 2012; Xu and others, 2012; Sun and others, 2014; Zhang and others, 2014; Cui and others, 2015; Zhao and others, 2016; Zhou and others, 2018). Thus, the presence of Archean crystalline basement, the nature of its lithospheric mantle, and the thermo-tectonic processes that formed these microcontinents, are still unclear.

We collected amphibolite and metadiorite samples from drill-hole ZK6301 of the Biliya Pb-Zn polymetallic deposit in the central-eastern Erguna Terrane (NE China; figs. 1B and 1C) and present data on their whole-rock geochemistry and Sm-Nd and Lu-Hf isotopes as well as zircon U-Pb age and Lu-Hf data. We discuss their magma source and the nature of their lithospheric mantle and crust extraction processes for these Neoarchean rocks of the CAOB.

GEOLOGICAL BACKGROUND AND SAMPLING

The eastern CAOB contains the Stannovoy, Erguna, Xing'an and Burean-Jiamusi microcontinental terranes (fig. 1A). Previous research on the Precambrian basement of these microcontinents focused on inferred Precambrian strata (for example, IMBGMR, 1991). However, recent high-precision detrital zircon dating revealed that the so called ''Precambrian'' rocks show Paleozoic and even Mesozoic maximum depositional ages (for example, Miao and others, 2007; Xie and others, 2008; Wu and others, 2012; Xu and others, 2012; Sun and others, 2014; Zhang and others, 2014; Cui and others, 2015; Zhao and others, 2016; Zhou and others, 2018). Detrital zircon data from sedimentary units within the terranes reveals similar age peaks at 495 Ma, 780 Ma, 1825 Ma and 2600 Ma to those reconized throughout the CAOB (Zhou and others, 2018). The eastern microcontinents within the CAOB share a common history to those identified elsewhere in the CAOB, including evidence for end Mesoproterozoic (~1000 Ma) and early Paleozoic (~500 Ma) orogenic events (Zhou and others, 2018). The Paleo-Asian Ocean dominated the Cambrian to Triassic tectonic evolution of the CAOB, and may have closed in the Late Permian to Early Triassic (Xiao and others, 2015). The tectonics of the eastern CAOB was also influenced by the Paleo-Pacific and Mongol-Okhotsk tectonic domains (Zhou and others, 2014; Wilde and Zhou, 2015). The Erguna Terrane is located between the Mongol-Okhotsk suture and Xinlin-Xiguitu-Toudaoqiao fault (fig. 1B) and is equivalent to the central Mongolia Terrane. Multiple Jurassic to Cretaceous volcanic and clastic units cover this terrane, including the Tamulangou, Manketouebo, Manitu, Baiyingaolao and Meiletu formations (fig. 2; IMBGMR, 1991). Permian to Cretaceous granitoids occur in a NE-SW trend across the terrane (fig. 1B).

The Derbuer ore field lies in central-eastern Erguna Terrane (NE China), and includes the De'rbuer, Erdaohezi and Jiawula-Chaganbuergen Ag-Pb-Zn polymetallic

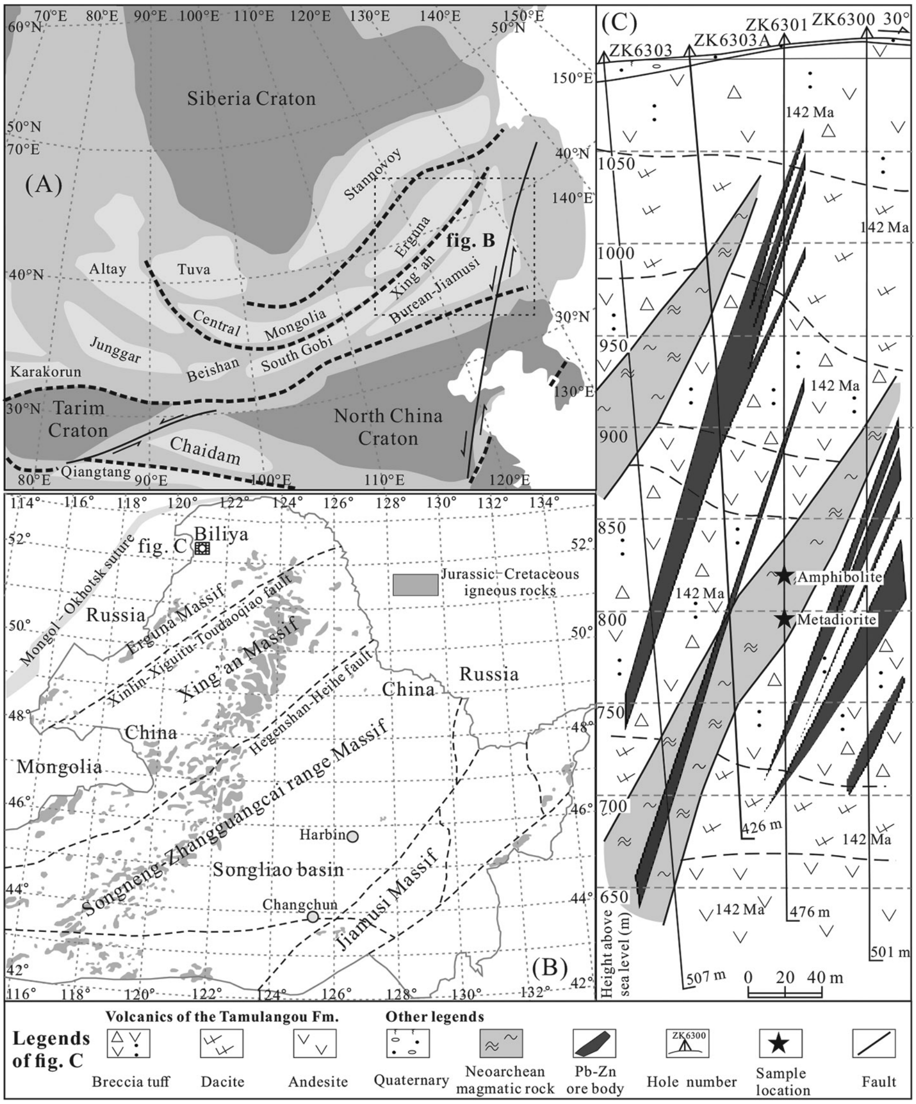

Fig. 1. (A) Simplified tectonic map showing the microcontinents distributions in the CAOB (modified after Zhou and others, 2018). (B) Schematic geological map of NE China (modified after Wu and others, 2011). U-Pb age data are from Gou and others (2013), Luan and others, (2019) and Yang and others (2017). (C) Geological cross-section of the Biliya Pb–Zn deposit in the Derbuer ore field.

deposits, Erentaolegai Ag deposit, and Biliya and Dongjun Pb-Zn polymetallic deposits (Zhao and others, 2018). The Biliya Pb-Zn polymetallic deposit (50°59′51.9″N, 120° 57′36.5″E) is located in a 3.5 km long and 650 to 720 m wide, NW trending fault zone (Zhao and others, 2018). About 50 ore bodies are distrbuted along a strike of 295° to 305° (dip 65°–85°; fig. 1C). Ore hosts are the volcanic rocks of the Tamulangou Formation (figs. 1C and 2), which comprise andesitic rocks (amygdaloidal/basaltic/augite andesite), dacite and breccia tuff. The Tamulangou Fm. volcanic rocks yield a zircon U-Pb age of 141.6 ± 1.8 Ma (Ming and others, 2015), and the sphalerite in Pb-Zn ores were dated by Rb-Sr at 141.6 ± 1.9 Ma (Zhao and others, 2017). Amphibolite

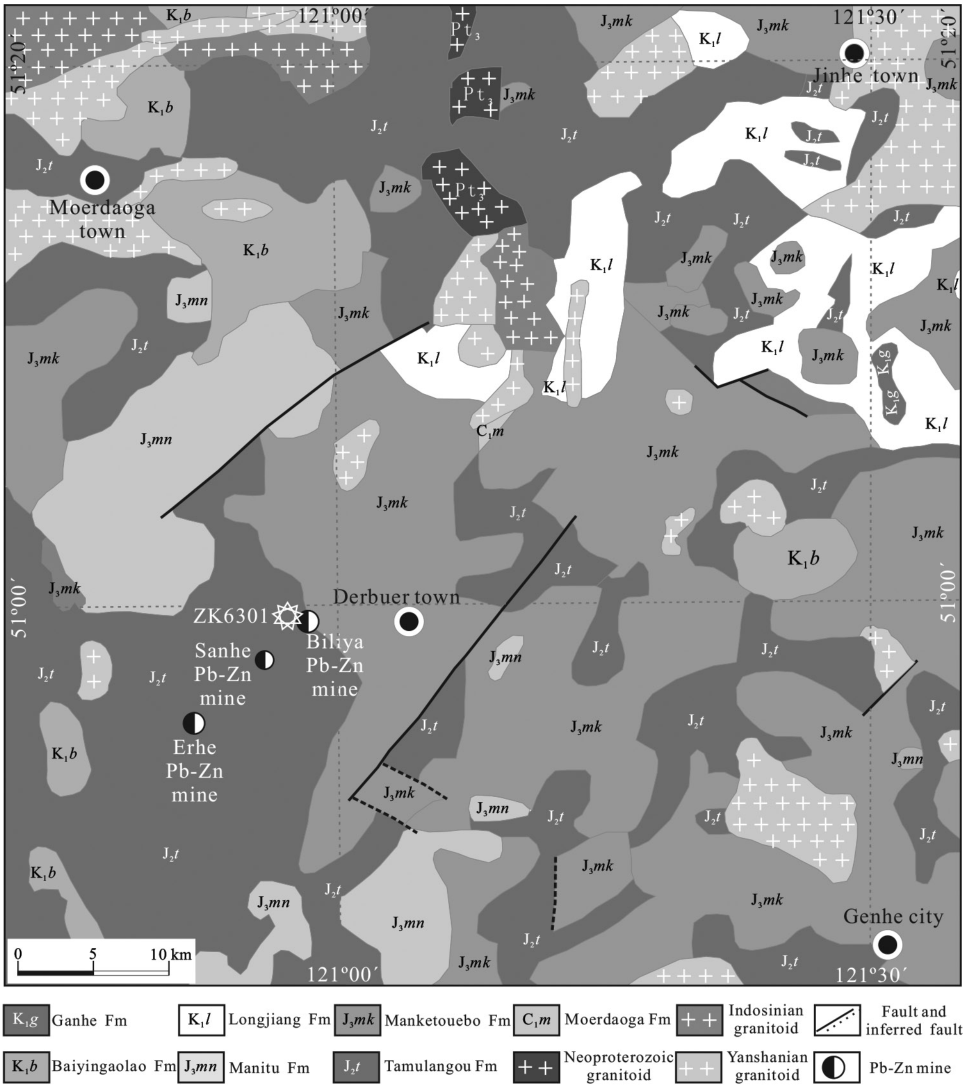

Fig. 2. Geological map showing the stratigraphic and igneous components of the Derbuer area (after IMBGMR, 1991).

and metadiorite were found in the four drill holes and they are in fault contact with the Tamulangou Formation (fig. 1C).

Six metadiorite (depth: 226 m) and nine amphibolite (depth: 198 m) samples were collected from the drill-hole ZK6301 at Biliya (figs. 1C and 2). The metadiorite samples comprise: (1) monzonitic two-mica schist (plagioclase + orthoclase + muscovite + biotite + quartz) with lepido-granoblastic texture (fig. 3A), (2) garnet two-mica quartz schist (plagioclase + muscovite + biotite + quartz + garnet) with porphyroblastic texture (fig. 3B), and (3) gneissic granodiorite with ~30 % andesine, ~25 % orthoclase, ~15 % quartz, ~15 % biotite, and ~5 % hornblende, along with the accessory minerals magnetite, zircon and apatite (figs. 3C and 3D). The amphibolite

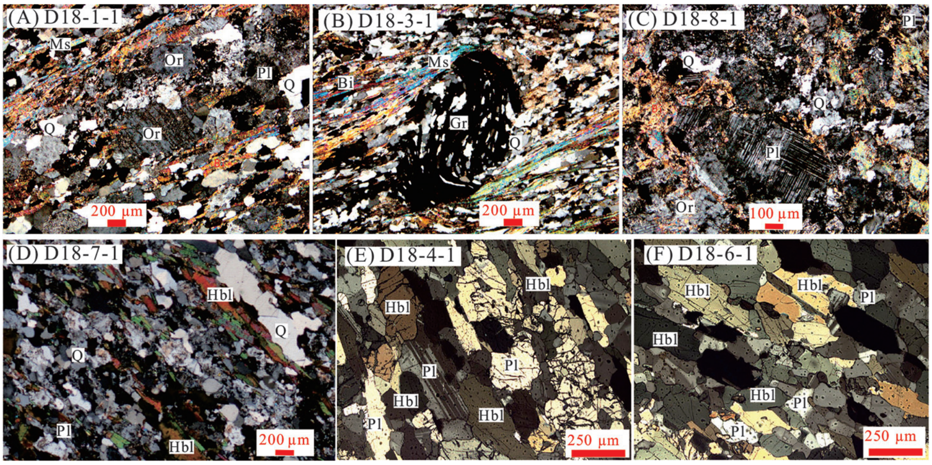

Fig. 3. Microphotoes of the monzonitic mica schist (A), garnet two-mica quartz schist (B), gneissic granodiorite (C–D), and amphibolite (E–F). Abbrevations: Pl – plagioclase, Or – orthoclase, Bi – biotite, Ms – muscovite, Gr – garnet, Hbl – hornblende.

samples contain ~75 % hornblende, ~20 % plagioclase, ~2 % quartz and the accessory minerals chlorite, epidote, magnetite, zircon and apatite (figs. 3E and 3F).

ANALYTICAL METHODS

Zircon U–Pb Dating and in situ Zircon Lu–Hf Isotope

Zircon mineral separates were prepared by conventional heavy liquid and magnetic techniques. Grains were mounted in epoxy, polished and coated with gold and then photographed in transmitted and reflected light. Their internal texture was examined using cathodoluminescence (CL) imaging at the Institute of Geology, Chinese Academy of Geological Sciences (CAGS), Beijing.

SHRIMP zircon U-Pb dating: For sample D18-1-1, zircon U-Pb dating was conducted using a sensitive high-resolution ion microprobe (SHRIMP II) at the Beijing SHRIMP Center, Institute of Geology, CAGS. Cathodoluminescence (CL) images were made on zircons prior to U-Th-Pb analyses to reveal the internal textures and to guide the SHRIMP analyses. Detailed analytical procedures are described by Jian and others (2012). Common Pb correction used the 204Pb method of Compston and others (1984). The SHRIMP analytical data presented are the mean values of five consecutive scans for each analytical spot. Errors quoted are at 1σ level, whereas weighted mean ages of samples are quoted at 2σ level.

LA-MC-ICPMS zircon U-Pb dating and *in situ* Lu-Hf isotopic analyses: For the four remaining samples (D18-2-1, D18-7-1, D18-3-1 and D18-6-1), U-Pb dating and trace element analysis of zircon were simultaneously conducted by LA-MC-ICPMS at the Wuhan Sample Solution Analytical Technology Co., Ltd., Wuhan, China. Detailed operating conditions for the laser ablation system and the ICP-MS instrument and data reduction are the same as description by Zong and others (2017). Zircon PLE and GJ-1 were used as external standards for U-Pb dating and trace element calibration, respectively. An Excel-based software ICPMSDataCal was used to perform off-line selection and integration of background and analyzed signals, time-drift correction and quantitative calibration for trace element analysis and U-Pb dating (Liu and others, 2010). Concordia diagrams and weighted mean calculations were made using Isoplot/Ex-ver2 (Ludwig, 2001). Zircon Lu-Hf isotopic analysis was carried out using the LA-MC-ICPMS. All the settings yielded a signal intensity of ~10 Vat 180Hf for the standard zircon 91500 with a recommended 176Hf/177Hf ratio of 0.282293 ± 28 (Wu and others, 2006). Data were normalized to 176Hf/177Hf = 0.7325, using exponential correction for mass bias. The ratio of 176Yb/172Yb (0.5887) was also applied for the Yb correction.

Whole–rock Element, Nd and Hf Isotope Determinations

Whole-rock major and trace elements: Whole rock samples for geochemistry were crushed to 200-mesh using an agate mill for major and trace element analyses. The major oxides were analyzed by a wavelength X-ray fluorescence spectrometry at the Wuhan Sample Solution Analytical Technology Co., Ltd., Wuhan, China. Trace element analyses were also performed at the same company by a Perkin-Elmer Sciex ELAN 6000 ICP-MS. Detailed sample preparation and analytical procedure followed Li and others (2002).

Whole-rock Nd and Hf isotopes: All chemical preparations were performed on class 100 work benches within a class 1000 over-pressured clean laboratory. Column chemistry: Both the Nd and Hf isotope analyses were performed on a Neptune Plus MC-ICP-MS (Thermo Fisher Scientific, Dreieich, Germany) at the Wuhan Sample Solution Analytical Technology Co., Ltd, Hubei, China. Details of analytical methods are presented by Yang and others (2006). Normalizing factors used to correct the mass fractionation of Nd during the measurements were 146Nd/144Nd= 0.7219 (Yang and others, 2005, 2006). For the Hf isotopes, mass discrimination correction was carried out via internal normalization to a 179Hf/177Hf ratio of 0.7325.

ANALYTICAL RESULTS

Geochronological and in situ Zircon Lu–Hf Isotopic Data

SHRIMP zircon U-Pb dating has been conducted on a metadiorite sample (D18-1-1) and LA-ICP-MS zircon U-Pb dating on two metadiorites samples (D18-2-1 and D18-7-1), and two amphibolite samples (D18-3-1 and D18-6-1). Detailed geochronological analytical results were listed in table 1. *In situ* zircon Lu-Hf isotopic analyses were conducted on these five dated samples, with the results listed in table 2.

Sample D18-1-1: Thirty spot analyses were performed on 30 zircon grains from the metadiorite sample using SHRIMP. The 30 analyzed zircon crystals are mainly euhedral with length of 60 to 150 μm and aspect ratios ranging from 1:1 to 2:1 (fig. 4A). Most of the zircons contain well-defined, broad sector zones that become thinner from core to rim. They show high Th (47–560 ppm) and U (94–765 ppm) contents, and high Th/U ratios (0.2 – 1.3; fig. 4G). These CL images and high Th/U ratios show typical features of igneous zircon (Hanchar and Miller, 1993). SHRIMP analyses on the magmatic cores plot on a discordia line with an upper concordia intercept age of 2481 ± 21 Ma (MSWD = 2.6, n = 30), which is consistent with the weighted mean 207Pb/206Pb age of the most concordant analyses: 2494 ± 61 Ma (MSWD = 0.07, n = 10; fig. 4A). This age (2481 ± 21 Ma) is interpreted as the magma crystallization age of the protolith. Twenty zircons from sample D18-1-1 have a limited range of initial 176Hf/177Hf ratios of 0.28118 to 0.28135 and εHf(t) values of −0.4 to +5.9 (fig. 5A). These values do not change with an increase in discordance, suggesting that the Lu–Hf system remained closed when Pb loss occurred. The two-staged model ages are in the range of 2642 Ma to 3043 Ma (table 2).

Sample D18-2-1: Twenty analyses have been carried out on 20 zircon grains from this metadiorite sample. The twenty zircon crystals are euhedral to subhedral and some fragmentary, with length between 80 and 150 μm, and contain broad cores and oscillatory thinner rims (fig. 4B). Our LA-ICPMS analyses concentrate in the cores and have high Th/U ratios of 0.2 to 0.9 (fig. 4G). These characteristics indicate an

TABLE 1

Zircon U–Pb analytical results of the Biliya amphibolite (Samples D18-1-1, D18-2-1 and D18-7-1) and metadiorite (Samples D18-3-1 and D18-6-1)

Samples	Th/U	$^{207}Pb/^{206}Pb$	2σ	$^{207}Pb/^{235}U$	2σ	$^{206}Pb/^{238}U$	2σ	$^{207}Pb/^{206}Pb$	2σ	$^{207}Pb/^{235}U$	2σ	$^{206}Pb/^{238}U$	2σ
D18-1-1-01	0.63	0.15780	0.00400	10.32630	0.30420	0.46760	0.01020	2432.4	43.7	2464.5	27.3	2473.0	44.8
D18-1-1-02	0.71	0.16510	0.00360	6.67700	0.18800	0.28790	0.00580	2509.3	37.0	2069.6	24.9	1631.1	28.9
D18-1-1-03	0.58	0.16340	0.00370	5.23320	0.16570	0.22870	0.00590	2491.1	37.2	1858.0	27.0	1327.6	31.2
D18-1-1-04	0.60	0.18150	0.00460	5.05770	0.14940	0.19960	0.00480	2666.4	41.4	1829.0	25.1	1173.0	25.5
D18-1-1-05	0.68	0.16690	0.00580	3.61160	0.20110	0.15220	0.00430	2526.9	53.2	1552.1	44.3	913.0	24.3
D18-1-1-06	0.74	0.15130	0.00380	4.69460	0.12860	0.22140	0.00380	2360.8	42.9	1766.3	23.0	1289.5	20.2
D18-1-1-07	0.83	0.16030	0.00360	10.55620	0.26580	0.47050	0.00790	2458.3	38.3	2484.9	23.4	2485.7	34.6
D18-1-1-08	0.58	0.15940	0.00540	4.61510	0.15410	0.20990	0.00620	2449.1	56.8	1752.0	27.9	1228.2	32.9
D18-1-1-09	0.43	0.16210	0.00450	5.23670	0.33070	0.23080	0.01340	2479.6	46.6	1858.6	53.8	1338.8	70.2
D18-1-1-10	0.67	0.16280	0.00440	8.95660	0.26390	0.39330	0.00720	2484.9	46.8	2333.6	27.0	2138.3	33.5
D18-1-1-11	0.43	0.15990	0.00420	6.83590	0.19090	0.30630	0.00540	2454.6	44.1	2090.4	24.8	1722.6	26.8
D18-1-1-12	0.68	0.16050	0.00370	10.41260	0.24580	0.46480	0.00650	2460.8	38.9	2472.2	21.9	2460.9	28.8
D18-1-1-13	0.70	0.15780	0.00370	5.61940	0.17350	0.25500	0.00610	2431.8	39.8	1919.1	26.7	1464.4	31.4
D18-1-1-14	0.66	0.15790	0.00360	10.13370	0.24270	0.46100	0.00640	2433.0	38.4	2447.1	22.2	2444.1	28.4
D18-1-1-15	0.58	0.15850	0.00430	6.69140	0.21790	0.30310	0.00650	2439.2	45.2	2071.5	28.8	1706.5	32.3
D18-1-1-16	0.67	0.15860	0.00470	8.68080	0.26510	0.39440	0.00770	2442.6	55.1	2305.1	27.9	2143.1	35.7
D18-1-1-17	0.50	0.16130	0.00430	5.01770	0.17470	0.22400	0.00610	2469.4	45.1	1822.3	29.5	1302.8	32.4
D18-1-1-18	0.59	0.16300	0.00430	10.50710	0.30960	0.46510	0.01160	2486.7	44.4	2480.5	27.4	2461.9	51.1
D18-1-1-19	0.84	0.21240	0.00560	7.05990	0.20670	0.23690	0.00310	2924.4	42.6	2119.0	26.1	1370.7	16.4
D18-1-1-20	0.52	0.15760	0.00410	6.06840	0.22350	0.27540	0.00800	2431.5	43.1	1985.7	32.1	1568.2	40.2
D18-1-1-21	0.68	0.16440	0.00420	10.74770	0.29020	0.47080	0.00890	2500.9	43.2	2501.6	25.1	2486.9	38.9
D18-1-1-22	1.26	0.16300	0.00380	5.36160	0.16130	0.23630	0.00550	2486.7	38.9	1878.7	25.8	1367.5	28.7
D18-1-1-23	0.80	0.17550	0.00400	12.16290	0.27840	0.49860	0.00630	2610.8	39.0	2617.1	21.5	2607.7	27.1
D18-1-1-24	0.49	0.18290	0.00520	12.61810	0.39140	0.49660	0.00980	2679.9	46.6	2651.6	29.2	2599.2	42.1
D18-1-1-25	1.09	0.18300	0.00530	12.67250	0.38530	0.49890	0.00830	2680.6	48.2	2655.6	28.7	2609.2	35.7
D18-1-1-26	0.61	0.16110	0.00440	5.85240	0.18920	0.26010	0.00480	2477.8	51.1	1954.2	28.1	1490.6	24.4
D18-1-1-27	0.73	0.16210	0.00390	6.48690	0.19290	0.28740	0.00570	2477.5	40.4	2044.1	26.2	1628.3	28.6
D18-1-1-28	0.41	0.16440	0.00380	5.19380	0.24260	0.22760	0.00950	2501.9	38.9	1851.6	39.8	1321.7	50.1
D18-1-1-29	0.19	0.17080	0.00410	3.77390	0.09490	0.15850	0.00200	2565.1	40.6	1587.2	20.2	948.3	11.2
D18-1-1-30	0.62	0.16490	0.00420	9.91120	0.25310	0.43270	0.00610	2505.9	44.0	2426.6	23.6	2318.0	27.6
D18-2-1-01	0.39	0.16021	0.00428	4.74800	0.14981	0.21228	0.00381	2457.7	44.6	1775.8	26.5	1241.0	20.3
D18-2-1-02	0.59	0.16628	0.00394	11.12043	0.25426	0.48107	0.00368	2520.7	40.6	2533.3	21.4	2531.9	16.1
D18-2-1-03	0.68	0.17532	0.00440	5.82485	0.14677	0.24011	0.00324	2609.0	40.9	1950.1	21.9	1387.3	16.9
D18-2-1-04	0.63	0.16791	0.00354	10.99063	0.23694	0.47212	0.00488	2536.7	35.5	2522.3	20.1	2492.8	21.4

Table 1
(continued)

Samples	Th/U	$^{207}Pb/^{206}Pb$	2σ	$^{207}Pb/^{235}U$	2σ	$^{206}Pb/^{238}U$	2σ	$^{207}Pb/^{206}Pb$	2σ	$^{207}Pb/^{235}U$	2σ	$^{206}Pb/^{238}U$	2σ
D18-2-1-05	0.28	0.16242	0.00355	5.94299	0.13410	0.26416	0.00276	2481.2	37.0	1967.5	19.7	1511.1	14.1
D18-2-1-06	0.45	0.26761	0.01338	13.23603	1.53039	0.28972	0.01833	3292.3	77.6	2696.6	109.2	1640.1	91.6
D18-2-1-07	0.72	0.16461	0.00385	4.92059	0.12192	0.21604	0.00250	2503.4	38.7	1805.8	20.9	1260.9	13.2
D18-2-1-08	0.76	0.16221	0.00333	8.62103	0.21351	0.38310	0.00540	2479.6	34.9	2298.8	22.6	2090.8	25.2
D18-2-1-09	0.84	0.16124	0.00321	7.75578	0.16278	0.34745	0.00342	2468.8	33.6	2203.1	18.9	1922.4	16.4
D18-2-1-10	0.92	0.16818	0.00311	11.65022	0.22107	0.50040	0.00443	2539.8	30.4	2576.7	17.8	2615.5	19.1
D18-2-1-11	0.70	0.16866	0.00313	11.38570	0.22948	0.48748	0.00540	2544.1	31.2	2555.3	18.9	2559.8	23.4
D18-2-1-12	0.67	0.16702	0.00332	12.09874	0.24501	0.52252	0.00437	2528.1	33.3	2612.1	19.1	2709.9	18.6
D18-2-1-13	0.18	0.17534	0.00379	7.55803	0.18807	0.31133	0.00494	2609.6	41.5	2179.9	22.4	1747.2	24.3
D18-2-1-14	0.86	0.16322	0.00347	11.32560	0.23083	0.50108	0.00417	2500.0	36.1	2550.3	19.1	2618.4	18.0
D18-2-1-15	0.78	0.16770	0.00328	9.28395	0.28175	0.39878	0.00944	2534.9	33.5	2366.4	27.9	2163.4	43.5
D18-2-1-16	0.63	0.17043	0.00318	12.76127	0.24443	0.54045	0.00490	2562.0	31.5	2662.2	18.1	2785.3	20.6
D18-2-1-17	0.74	0.16190	0.00309	2.54135	0.06508	0.11336	0.00219	2475.6	33.2	1284.0	18.7	692.2	12.7
D18-2-1-18	0.80	0.15689	0.00299	5.97266	0.12428	0.27503	0.00331	2433.3	31.9	1971.9	18.1	1566.3	16.7
D18-2-1-19	0.49	0.15410	0.00320	4.68217	0.12304	0.21962	0.00407	2391.7	30.6	1764.1	22.0	1279.9	21.5
D18-2-1-20	0.89	0.15405	0.00343	4.63909	0.10860	0.21779	0.00278	2391.7	38.0	1756.3	19.6	1270.2	14.7
D18-7-1-01	0.71	0.17538	0.00671	12.11070	0.44124	0.49634	0.00741	2609.6	62.8	2613.0	34.2	2598.0	31.9
D18-7-1-02	0.87	0.16582	0.00502	11.45901	0.33065	0.49356	0.00543	2515.7	50.9	2561.2	27.0	2586.1	23.5
D18-7-1-03	0.71	0.15963	0.00480	6.42234	0.19576	0.28750	0.00444	2451.5	50.9	2035.3	26.8	1629.0	22.2
D18-7-1-04	0.87	0.16885	0.00473	10.69111	0.31680	0.45163	0.00716	2546.0	46.9	2496.7	27.6	2402.5	31.8
D18-7-1-05	0.90	0.17450	0.00533	9.14772	0.26225	0.37514	0.00419	2601.5	50.9	2352.9	26.3	2053.5	19.7
D18-7-1-06	0.73	0.14888	0.00513	2.96908	0.14893	0.14182	0.00531	2333.0	59.3	1399.7	38.1	854.9	30.0
D18-7-1-07	0.87	0.15891	0.00527	8.09416	0.28643	0.36427	0.00706	2444.1	56.2	2241.6	32.0	2002.4	33.4
D18-7-1-08	0.59	0.17186	0.00542	11.91721	0.36800	0.49615	0.00558	2575.6	51.7	2597.9	29.0	2597.2	24.1
D18-7-1-09	0.80	0.15522	0.00456	5.90184	0.17722	0.27303	0.00424	2405.6	50.0	1961.5	26.1	1556.2	21.5
D18-7-1-10	0.75	0.16640	0.00458	12.06617	0.33647	0.52080	0.00646	2521.9	46.3	2609.6	26.2	2702.6	27.4
D18-7-1-11	0.92	0.15982	0.00455	10.68882	0.28783	0.48101	0.00503	2454.0	48.1	2496.5	25.1	2531.6	22.0
D18-7-1-12	0.64	0.16103	0.00475	10.49351	0.32050	0.46837	0.00651	2466.4	50.0	2479.3	28.4	2476.4	28.6
D18-7-1-13	0.76	0.16667	0.00586	12.51679	0.43678	0.54171	0.00739	2524.4	59.4	2644.0	32.9	2790.6	30.9
D18-7-1-14	0.69	0.17136	0.00562	12.30396	0.40946	0.51613	0.00684	2572.2	54.2	2627.9	31.3	2682.8	29.1
D18-7-1-15	0.46	0.15816	0.00506	4.39960	0.15534	0.20005	0.00408	2436.1	59.7	1712.3	29.2	1175.6	21.9
D18-7-1-16	0.72	0.16893	0.00498	9.20879	0.31282	0.39165	0.00847	2547.2	48.6	2359.0	31.2	2130.5	39.3
D18-7-1-17	0.62	0.14966	0.00407	4.04436	0.14170	0.19216	0.00420	2342.3	46.6	1643.2	28.5	1133.1	22.7
D18-7-1-18	0.70	0.16306	0.00469	9.94490	0.29124	0.43722	0.00708	2488.0	48.5	2429.7	27.1	2338.2	31.8
D18-7-1-19	0.61	0.16095	0.00486	5.95097	0.18016	0.26465	0.00432	2465.7	51.4	1968.7	26.4	1513.6	22.0

Table 1
(continued)

Samples	Th/U	$^{207}Pb/^{206}Pb$	2σ	$^{207}Pb/^{235}U$	2σ	$^{206}Pb/^{238}U$	2σ	$^{207}Pb/^{206}Pb$	2σ	$^{207}Pb/^{235}U$	2σ	$^{206}Pb/^{238}U$	2σ
D18-7-1-20	0.69	0.15785	0.00502	8.23613	0.32448	0.37117	0.00979	2433.0	49.1	2257.3	35.7	2034.9	46.1
D18-3-1-01	0.43	0.15901	0.00350	6.96429	0.16320	0.31668	0.00402	2455.6	37.0	2106.9	20.9	1773.5	19.7
D18-3-1-02	0.54	0.16439	0.00328	11.23745	0.23722	0.49344	0.00518	2501.5	28.2	2543.0	19.8	2585.5	22.4
D18-3-1-03	0.89	0.17176	0.00335	9.02528	0.18338	0.37895	0.00325	2575.9	32.7	2340.6	18.6	2071.4	15.2
D18-3-1-04	0.85	0.16636	0.00348	9.13651	0.20712	0.39672	0.00509	2521.3	39.8	2351.8	20.8	2153.9	23.5
D18-3-1-05	0.88	0.16744	0.00377	9.64299	0.23204	0.41631	0.00554	2532.4	37.7	2401.3	22.2	2243.7	25.3
D18-3-1-06	0.59	0.16777	0.00392	10.43827	0.24822	0.44933	0.00502	2535.5	40.0	2474.5	22.1	2392.3	22.4
D18-3-1-07	0.61	0.17058	0.00420	10.08269	0.25447	0.42720	0.00532	2564.8	42.1	2442.4	23.4	2293.1	24.1
D18-3-1-08	0.90	0.16811	0.00356	7.75205	0.16494	0.33274	0.00302	2539.2	35.5	2202.7	19.2	1851.7	14.6
D18-3-1-09	0.77	0.17316	0.00347	10.25113	0.21807	0.42766	0.00527	2588.6	33.3	2457.7	19.8	2295.1	23.8
D18-3-1-10	0.96	0.17564	0.00358	9.39738	0.23258	0.38448	0.00508	2612.0	34.3	2377.6	22.8	2097.2	23.7
D18-3-1-11	0.72	0.16822	0.00332	11.42763	0.23040	0.48966	0.00406	2539.8	33.0	2558.7	18.9	2569.2	17.6
D18-3-1-12	0.82	0.16744	0.00379	7.86147	0.21861	0.33995	0.00696	2532.4	38.0	2215.3	25.1	1886.4	33.5
D18-3-1-13	0.63	0.16775	0.00387	12.19161	0.29197	0.52320	0.00510	2535.5	38.9	2619.3	22.5	2712.7	21.6
D18-3-1-14	0.60	0.16568	0.00402	7.17665	0.18260	0.31190	0.00360	2514.5	40.7	2133.6	22.7	1750.0	17.7
D18-3-1-15	0.66	0.16438	0.00372	11.43358	0.28733	0.50029	0.00633	2500.9	38.0	2559.2	23.5	2615.0	27.2
D18-3-1-16	0.86	0.16494	0.00368	11.29547	0.24869	0.49359	0.00426	2507.1	37.7	2547.8	20.6	2586.2	18.5
D18-3-1-17	0.75	0.16745	0.00333	12.30614	0.24884	0.52920	0.00465	2532.4	33.3	2628.0	19.1	2738.1	19.7
D18-3-1-18	0.78	0.16344	0.00330	11.56832	0.22701	0.51010	0.00399	2491.7	34.0	2570.1	18.4	2657.1	17.1
D18-3-1-19	1.23	0.16438	0.00317	12.31539	0.23030	0.53988	0.00435	2500.9	32.4	2628.7	17.7	2782.9	18.3
D18-3-1-20	0.90	0.16529	0.00335	9.73832	0.19959	0.42451	0.00417	2510.8	34.0	2410.3	18.9	2280.9	18.9
D18-6-1-01	0.65	0.16152	0.00464	8.85085	0.28556	0.39202	0.00856	2471.3	43.5	2322.7	29.5	2132.2	39.6
D18-6-1-02	0.73	0.16633	0.00435	11.95478	0.30806	0.51319	0.00566	2521.3	44.1	2600.9	24.2	2670.2	24.2
D18-6-1-03	0.68	0.17200	0.00468	12.79324	0.33815	0.53251	0.00587	2577.5	45.4	2664.5	25.0	2752.0	24.7
D18-6-1-04	0.74	0.16841	0.00460	8.13806	0.30182	0.34440	0.00892	2541.7	45.7	2246.5	33.6	1907.8	42.8
D18-6-1-05	0.54	0.16597	0.00471	6.32709	0.18472	0.27305	0.00365	2517.6	47.8	2022.2	25.6	1556.3	18.5
D18-6-1-06	0.53	0.17403	0.00541	9.62817	0.32379	0.39681	0.00723	2598.2	51.9	2399.9	31.0	2154.3	33.4
D18-6-1-07	0.67	0.17923	0.00580	9.72224	0.30788	0.39060	0.00546	2646.0	53.7	2408.8	29.2	2125.6	25.4
D18-6-1-08	0.72	0.17270	0.00539	10.41909	0.32171	0.43459	0.00630	2584.3	51.9	2472.7	28.7	2326.4	28.3
D18-6-1-09	0.56	0.16704	0.00481	10.73094	0.31281	0.46189	0.00568	2528.1	48.2	2500.1	27.1	2447.9	25.1
D18-6-1-10	0.79	0.17453	0.00491	11.35148	0.31167	0.46789	0.00463	2601.5	46.9	2552.4	25.7	2474.3	20.4
D18-6-1-11	0.60	0.17531	0.00551	12.75297	0.38977	0.52525	0.00676	2609.0	46.8	2661.6	28.8	2721.4	28.6
D18-6-1-12	0.62	0.16877	0.00563	8.52906	0.29507	0.36402	0.00614	2545.4	61.3	2289.0	31.5	2001.2	29.1
D18-6-1-13	0.90	0.16785	0.00576	11.67735	0.40795	0.49985	0.00610	2536.1	58.5	2578.9	32.7	2613.2	26.3

TABLE 1

(continued)

Samples	Th/U	$^{207}Pb/^{206}Pb$	2σ	$^{207}Pb/^{235}U$	2σ	$^{206}Pb/^{238}U$	2σ	$^{207}Pb/^{206}Pb$	2σ	$^{207}Pb/^{235}U$	2σ	$^{206}Pb/^{238}U$	2σ
D18-7-1-20	0.69	0.15785	0.00502	8.23613	0.32448	0.37117	0.00979	2433.0	49.1	2257.3	35.7	2034.9	46.1
D18-6-1-14	0.72	0.16178	0.00561	6.04932	0.24938	0.26840	0.00642	2475.9	58.6	1983.0	35.9	1532.7	32.6
D18-6-1-15	0.62	0.16914	0.00535	11.80579	0.37221	0.50268	0.00579	2549.1	52.8	2589.1	29.6	2625.3	24.9
D18-6-1-16	0.90	0.16751	0.00494	11.50607	0.34429	0.49450	0.00569	2533.0	50.5	2565.1	28.0	2590.1	24.6
D18-6-1-17	0.85	0.05660	0.01617	3.23449	0.67272	0.25154	0.00744	476.0	533.3	1465.5	161.3	1446.4	38.3
D18-6-1-18	0.96	0.42498	0.01342	33.67022	4.55918	0.49549	0.05158	3999.8	46.4	3600.4	133.5	2594.4	222.3
D18-6-1-19	0.60	0.16174	0.00447	9.30105	0.26023	0.41403	0.00487	2473.8	46.1	2368.1	25.7	2233.3	22.2
D18-6-1-20	0.42	0.16276	0.00470	11.19395	0.32137	0.49472	0.00516	2484.3	48.8	2539.4	26.8	2591.1	22.3

Table 2

In-situ zircon Lu-Hf analytical results of the Biliya amphibolite (Samples D18-1-1, D18-2-1 and D18-7-1) and metadiorite (Samples D18-3-1 and D18-6-1)

Samples	Age (Ma)	$^{176}Yb/^{177}Hf$	2σ	$^{176}Lu/^{177}Hf$	2σ	$^{176}Hf/^{177}Hf$	2σ	$^{176}Hf/^{177}Hf_i$	$\varepsilon_{Hf}(0)$	$\varepsilon_{Hf}(t)$	T_{DM}(Ma)	T_{DM}^C(Ma)	$f_{Lu/Hf}$
D18-1-1-01	2481	0.02353	0.00032	0.00084	0.00001	0.28128	0.00002	0.28124	-52.7	1.5	2738	2893	-0.97
D18-1-1-02	2481	0.02954	0.00025	0.00107	0.00001	0.28128	0.00002	0.28123	-52.7	1.1	2754	2916	-0.97
D18-1-1-03	2481	0.02362	0.00047	0.00090	0.00001	0.28125	0.00002	0.28121	-53.8	0.3	2787	2971	-0.97
D18-1-1-04	2481	0.02375	0.00037	0.00088	0.00001	0.28132	0.00002	0.28128	-51.4	2.7	2692	2819	-0.97
D18-1-1-05	2481	0.03689	0.00112	0.00131	0.00004	0.28135	0.00002	0.28128	-50.5	3.0	2685	2804	-0.96
D18-1-1-06	2481	0.02138	0.00061	0.00083	0.00003	0.28126	0.00002	0.28122	-53.4	0.8	2764	2936	-0.98
D18-1-1-07	2481	0.02185	0.00078	0.00082	0.00003	0.28128	0.00002	0.28124	-52.9	1.3	2746	2907	-0.98
D18-1-1-08	2481	0.03042	0.00107	0.00106	0.00003	0.28132	0.00002	0.28127	-51.3	2.6	2699	2830	-0.97
D18-1-1-09	2481	0.02230	0.00059	0.00083	0.00003	0.28126	0.00002	0.28122	-53.6	0.6	2772	2948	-0.97
D18-1-1-10	2481	0.02634	0.00069	0.00094	0.00002	0.28132	0.00002	0.28127	-51.4	2.6	2697	2827	-0.97
D18-1-1-11	2481	0.03297	0.00106	0.00119	0.00002	0.28134	0.00002	0.28128	-50.8	2.9	2689	2812	-0.96
D18-1-1-12	2481	0.02440	0.00058	0.00091	0.00003	0.28130	0.00002	0.28126	-52.1	2.0	2720	2863	-0.97
D18-1-1-13	2481	0.02509	0.00028	0.00093	0.00001	0.28130	0.00002	0.28125	-52.1	1.9	2723	2868	-0.97
D18-1-1-14	2481	0.02293	0.00018	0.00089	0.00001	0.28127	0.00002	0.28123	-53.2	1.0	2760	2928	-0.97
D18-1-1-15	2481	0.02385	0.00028	0.00091	0.00001	0.28122	0.00002	0.28118	-54.9	-0.8	2827	3035	-0.97
D18-1-1-16	2481	0.02635	0.00020	0.00097	0.00001	0.28131	0.00002	0.28126	-51.8	2.2	2712	2850	-0.97
D18-1-1-17	2481	0.06071	0.00360	0.00200	0.00011	0.28145	0.00003	0.28135	-46.8	5.4	2592	2653	-0.94
D18-1-1-18	2481	0.02310	0.00052	0.00087	0.00002	0.28131	0.00002	0.28127	-51.7	2.5	2702	2836	-0.97
D18-1-1-19	2481	0.03338	0.00060	0.00122	0.00003	0.28134	0.00002	0.28129	-50.5	3.1	2682	2800	-0.96
D18-1-1-20	2481	0.02522	0.00040	0.00089	0.00001	0.28130	0.00002	0.28125	-52.2	1.9	2722	2867	-0.97
D18-2-1-1	2539	0.01793	0.00060	0.00068	0.00002	0.28126	0.00002	0.28122	-53.6	2.2	2762	2898	-0.98
D18-2-1-2	2539	0.02448	0.00020	0.00085	0.00000	0.28141	0.00002	0.28137	-48.1	7.4	2564	2579	-0.97
D18-2-1-3	2539	0.03990	0.00271	0.00137	0.00007	0.28135	0.00002	0.28128	-50.2	4.4	2681	2764	-0.96
D18-2-1-4	2539	0.02563	0.00028	0.00095	0.00001	0.28129	0.00002	0.28125	-52.3	3.0	2732	2849	-0.97
D18-2-1-5	2539	0.03851	0.00420	0.00114	0.00010	0.28135	0.00003	0.28129	-50.4	4.7	2669	2746	-0.97
D18-2-1-6	2539	0.06876	0.00122	0.00202	0.00003	0.28147	0.00002	0.28138	-45.9	7.6	2557	2566	-0.94
D18-2-1-7	2539	0.02401	0.00071	0.00084	0.00002	0.28127	0.00002	0.28123	-53.1	2.5	2752	2881	-0.97
D18-2-1-8	2539	0.03410	0.00055	0.00124	0.00002	0.28131	0.00002	0.28125	-51.7	3.1	2728	2840	-0.96
D18-2-1-9	2539	0.03679	0.00210	0.00122	0.00006	0.28135	0.00002	0.28129	-50.4	4.5	2676	2756	-0.96
D18-2-1-10	2539	0.03248	0.00039	0.00115	0.00002	0.28130	0.00002	0.28125	-51.9	3.0	2731	2845	-0.97
D18-2-1-11	2539	0.03743	0.00097	0.00130	0.00005	0.28133	0.00003	0.28126	-51.2	3.6	2712	2813	-0.96
D18-2-1-12	2539	0.01103	0.00005	0.00042	0.00000	0.28120	0.00002	0.28118	-55.5	0.8	2813	2984	-0.99
D18-2-1-13	2539	0.02018	0.00018	0.00073	0.00002	0.28132	0.00003	0.28128	-51.4	4.3	2682	2770	-0.98

TABLE 2

(continued)

Samples	Age (Ma)	$^{176}Yb/^{177}Hf$	2σ	$^{176}Lu/^{177}Hf$	2σ	$^{176}Hf/^{177}Hf$	2σ	$^{176}Hf/^{177}Hf_i$	$\varepsilon_{Hf}(0)$	$\varepsilon_{Hf}(t)$	T_{DM}(Ma)	T_{DM}^C(Ma)	$f_{Lu/Hf}$
D18-2-1-14	2539	0.02344	0.00111	0.00079	0.00003	0.28133	0.00002	0.28129	-51.1	4.5	2672	2753	-0.98
D18-2-1-15	2539	0.02968	0.00049	0.00106	0.00001	0.28129	0.00002	0.28124	-52.4	2.7	2745	2867	-0.97
D18-2-1-16	2539	0.01641	0.00021	0.00056	0.00000	0.28126	0.00002	0.28124	-53.3	2.6	2743	2870	-0.98
D18-2-1-17	2539	0.03151	0.00077	0.00114	0.00003	0.28126	0.00002	0.28120	-53.5	1.5	2792	2942	-0.97
D18-2-1-18	2539	0.05117	0.00270	0.00161	0.00006	0.28139	0.00003	0.28131	-49.0	5.2	2648	2711	-0.95
D18-2-1-19	2539	0.02384	0.00066	0.00088	0.00003	0.28127	0.00002	0.28123	-53.2	2.3	2759	2892	-0.97
D18-2-1-20	2539	0.03100	0.00048	0.00103	0.00001	0.28130	0.00002	0.28125	-52.2	3.0	2732	2847	-0.97
D18-7-1-1	2539	0.02284	0.00022	0.00083	0.00001	0.28136	0.00002	0.28132	-50.0	5.5	2634	2692	-0.98
D18-7-1-2	2539	0.02103	0.00083	0.00073	0.00003	0.28128	0.00002	0.28125	-52.7	3.0	2730	2847	-0.98
D18-7-1-3	2539	0.02425	0.00064	0.00100	0.00004	0.28129	0.00002	0.28125	-52.2	3.0	2732	2848	-0.97
D18-7-1-4	2539	0.02790	0.00036	0.00109	0.00002	0.28126	0.00003	0.28120	-53.5	1.5	2789	2938	-0.97
D18-7-1-5	2539	0.03070	0.00036	0.00112	0.00002	0.28137	0.00002	0.28132	-49.6	5.4	2639	2698	-0.97
D18-7-1-6	2539	0.05111	0.00191	0.00166	0.00005	0.28142	0.00002	0.28134	-47.9	6.2	2610	2651	-0.95
D18-7-1-7	2539	0.02716	0.00080	0.00101	0.00004	0.28133	0.00003	0.28128	-51.1	4.1	2690	2780	-0.97
D18-7-1-8	2539	0.02561	0.00070	0.00095	0.00002	0.28130	0.00002	0.28125	-52.1	3.2	2724	2834	-0.97
D18-7-1-9	2539	0.03559	0.00080	0.00135	0.00004	0.28132	0.00003	0.28126	-51.3	3.3	2721	2827	-0.96
D18-7-1-10	2539	0.03819	0.00086	0.00146	0.00005	0.28136	0.00004	0.28129	-50.0	4.4	2680	2761	-0.96
D18-3-1-11	2537	0.01213	0.00074	0.00048	0.00003	0.28123	0.00002	0.28121	-54.5	1.6	2781	2933	-0.99
D18-3-1-12	2537	0.02609	0.00051	0.00096	0.00001	0.28130	0.00002	0.28126	-51.9	3.4	2717	2825	-0.97
D18-3-1-13	2537	0.02412	0.00015	0.00081	0.00002	0.28128	0.00002	0.28124	-52.7	2.9	2735	2855	-0.98
D18-3-1-14	2537	0.02651	0.00069	0.00097	0.00002	0.28123	0.00002	0.28118	-54.6	0.6	2822	2993	-0.97
D18-3-1-15	2537	0.03260	0.00056	0.00106	0.00002	0.28131	0.00002	0.28126	-51.8	3.3	2720	2829	-0.97
D18-3-1-16	2537	0.03124	0.00036	0.00111	0.00001	0.28123	0.00002	0.28117	-54.7	0.3	2834	3011	-0.97
D18-3-1-17	2537	0.02836	0.00153	0.00094	0.00004	0.28128	0.00002	0.28123	-52.9	2.4	2754	2885	-0.97
D18-3-1-18	2537	0.04164	0.00065	0.00132	0.00003	0.28136	0.00002	0.28129	-50.0	4.6	2668	2745	-0.96
D18-3-1-19	2537	0.03852	0.00038	0.00148	0.00002	0.28140	0.00004	0.28133	-48.6	5.8	2625	2675	-0.96
D18-3-1-20	2537	0.02953	0.00099	0.00109	0.00002	0.28127	0.00002	0.28122	-53.0	2.1	2766	2903	-0.97
D18-6-1-1	2565	0.01292	0.00016	0.00050	0.00000	0.28119	0.00002	0.28117	-55.9	0.7	2837	3005	-0.98
D18-6-1-2	2565	0.01516	0.00013	0.00060	0.00000	0.28123	0.00002	0.28120	-54.4	2.1	2787	2923	-0.98
D18-6-1-3	2565	0.02363	0.00014	0.00089	0.00000	0.28127	0.00002	0.28123	-53.1	2.9	2757	2874	-0.97
D18-6-1-4	2565	0.02408	0.00017	0.00084	0.00001	0.28125	0.00002	0.28121	-53.7	2.4	2778	2907	-0.97
D18-6-1-5	2565	0.02067	0.00038	0.00069	0.00001	0.28125	0.00002	0.28121	-53.9	2.5	2773	2901	-0.98
D18-6-1-6	2565	0.01332	0.00032	0.00051	0.00001	0.28125	0.00002	0.28123	-53.8	2.9	2757	2876	-0.98
D18-6-1-7	2565	0.01391	0.00052	0.00054	0.00002	0.28123	0.00002	0.28120	-54.6	2.1	2788	2926	-0.98
D18-6-1-8	2565	0.01710	0.00021	0.00065	0.00000	0.28126	0.00002	0.28123	-53.5	2.9	2755	2872	-0.98

TABLE 2

(continued)

Samples	Age (Ma)	$^{176}Yb/^{177}Hf$	2σ	$^{176}Lu/^{177}Hf$	2σ	$^{176}Hf/^{177}Hf$	2σ	$^{176}Hf/^{177}Hf_i$	$\varepsilon_{Hf}(0)$	$\varepsilon_{Hf}(t)$	T_{DM}(Ma)	T_{DM}^C(Ma)	$f_{Lu/Hf}$
D18-6-1-9	2565	0.02344	0.00035	0.00087	0.00001	0.28125	0.00002	0.28121	-53.9	2.2	2786	2919	-0.97
D18-6-1-10	2565	0.02413	0.00016	0.00093	0.00001	0.28128	0.00002	0.28123	-52.8	3.2	2748	2858	-0.97
D18-6-1-11	2565	0.01946	0.00051	0.00077	0.00002	0.28125	0.00003	0.28121	-53.8	2.4	2774	2902	-0.98
D18-6-1-12	2565	0.02870	0.00056	0.00096	0.00001	0.28127	0.00002	0.28123	-53.0	2.9	2758	2874	-0.97
D18-6-1-13	2565	0.01769	0.00024	0.00068	0.00001	0.28127	0.00002	0.28123	-53.3	3.1	2749	2862	-0.98
D18-6-1-14	2565	0.01794	0.00140	0.00065	0.00005	0.28131	0.00002	0.28127	-51.8	4.6	2692	2771	-0.98
D18-6-1-15	2565	0.02313	0.00039	0.00086	0.00001	0.28129	0.00002	0.28125	-52.4	3.6	2729	2828	-0.97
D18-6-1-16	2565	0.01985	0.00015	0.00075	0.00001	0.28126	0.00002	0.28122	-53.5	2.7	2764	2885	-0.98
D18-6-1-17	2565	0.02915	0.00019	0.00109	0.00001	0.28133	0.00002	0.28128	-50.8	4.8	2685	2756	-0.97
D18-6-1-18	2565	0.01621	0.00017	0.00061	0.00001	0.28128	0.00002	0.28125	-52.9	3.6	2730	2832	-0.98
D18-6-1-19	2565	0.03925	0.00099	0.00129	0.00003	0.28142	0.00003	0.28136	-47.7	7.7	2575	2581	-0.96
D18-6-1-20	2565	0.02162	0.00020	0.00079	0.00001	0.28124	0.00002	0.28120	-54.1	2.0	2790	2927	-0.98

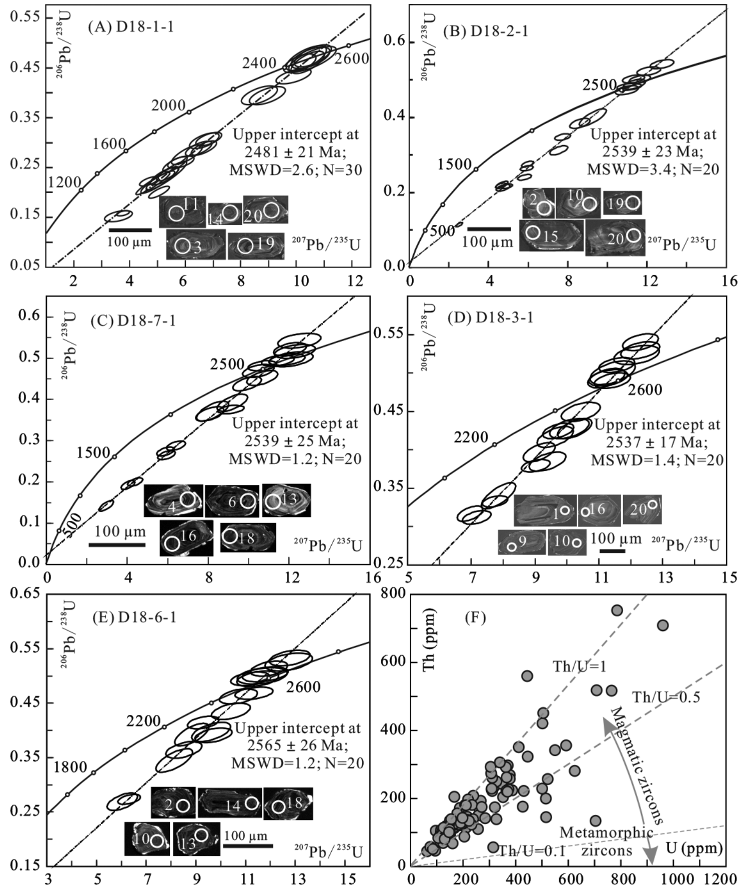

Fig. 4. (A) SHRIMP zircon U-Pb Concordia diagram. (B–E) LA-ICP-MS zircon U-Pb Concordia diagrams. (F) Th and U contents of the analyzed zircons.

igneous origin (Hanchar and Miller, 1993). The magmatic cores yielded an upper concordia intercept age of 2539 ± 23 Ma (MSWD = 3.4, n = 20) and a weighted mean 207Pb/206Pb age of 2529 ± 18 Ma (MSWD = 0.87, n = 6; fig. 4B). This age (2539 ± 23 Ma) represents the magma crystallization age of the protolith. Twenty *in situ* Lu-Hf analyses were recalculated to this crystallization age. They show initial 176Hf/177Hf ratios of 0.28118 to 0.28138 and εHf(t) values of −0.1 to +6.7 (fig. 5A). The two-staged model ages are in the range of 2588 Ma to 3009 Ma.

Sample D18-7-1: Twenty analyses have been carried out on 20 zircon grains from this metadiorite sample. The twenty zircon crystals are euhedral to subhedral, with length between 60 and 110 μm, and contain broad cores and oscillatory thinner rims (fig. 4C). The bright metamorphic rims are too narrow to be analyzed by LA-ICPMS. Our analyses concentrate at the cores and show high Th/U ratios of 0.5 to 0.9 (fig. 4G). These characteristics indicate an igneous origin (Hanchar and Miller, 1993). The magmatic cores define an upper intercept age of 2539 ± 25 Ma (MSWD = 1.2, n = 20) and a weighted mean 207Pb/206Pb age of 2527 ± 35 Ma (MSWD = 1.5, n = 10; fig. 4C), with the former age (2539 ± 25 Ma) taken as the magma crystallization age of the granodiorite. Twenty *in situ* Lu-Hf analyses were recalculated to this crystallization

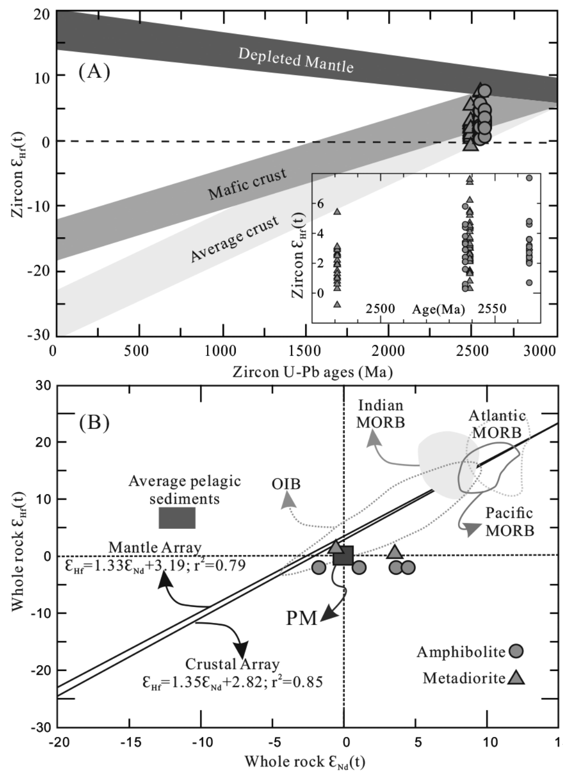

Fig. 5. U-Pb ages (Ma) vs. zircon εHf(t) values (A) and whole-rock εNd(t) vs. whole-rock εHf(t) values (B). Shaded areas in (A) are from Yang and others (2008). The mantle and crustal arrays are from Albarède and others (2000) and Vervoort and others (2000). The MORB and OIB fields are from Georoc (http://georoc.mpch-mainz.gwdg.de/georoc/).

age. They show initial 176Hf/177Hf ratios of 0.28117 to 0.28134 and εHf(t) values of –0.6 to +5.4 (fig. 5A). The two-staged model ages are in the range of 2673 Ma to 3037 Ma.

Sample D18-3-1: Twenty analyses were performed on 20 zircon grains. The 20 spots display well-preserved euhedral growth zones and oscillatory zoning, with length between 100 and 180 μm and aspect ratios of 1:1 to 2:1 (fig. 4D). They show high Th/U ratios of 0.4 to 1.2 (fig. 4G and table 1), indicative of a magmatic origin (Hanchar and Miller, 1993). Analyses of these zircons gave an upper intercept age of 2537 ± 17 Ma (MSWD = 1.4, n = 20), and a weighted mean 207Pb/206Pb age of 2510 ± 18 Ma (MSWD = 0.7, n = 7; fig. 4D). This age (2537 ± 17 Ma) represents the magma crystallization age of the protolith. Twenty *in situ* Lu-Hf analyses were recalculated to this crystallization age. They show initial 176Hf/177Hf ratios of 0.28117 to 0.28133 and εHf(t) values of −0.5 to +5.0 (fig. 5A). The two-staged model ages are in the range of 2697 Ma to 3033 Ma.

Sample D18-6-1: Twenty analyses were performed on 20 zircon grains. The 20 spots display well-preserved euhedral growth zones and oscillatory zoning, with length between 80 and 150 μm and aspect ratios of 1:1 to 3:1 (fig. 4E). They show high Th/U ratios of 0.4 to 1.0 (fig. 4G and table 1), which indicates a magmatic origin (Hanchar and Miller, 1993). They gave an upper intercept age of 2565 ± 26 Ma (MSWD = 1.2, n = 20), and a weighted mean 207Pb/206Pb age of 2549 ± 32 Ma (MSWD = 1.3, n = 9; fig. 4E), and the former age is taken as the crystallization age of the protolith. Twenty *in situ* Lu-Hf analyses were recalculated to this crystallization age. They show initial

176Hf/177Hf ratios of 0.28117 to 0.28136 and εHf(t) values of −0.7 to +6.2 (fig. 5A). The two-staged model ages are in the range of 2619 Ma to 3046 Ma.

Geochemical Analytical Results

Nine amphibolite and six metadiorite samples were analyzed for their major and trace element compositions, and the results are listed in table 3. The amphibolite samples have SiO2 = 44.24–51.12 wt.%, Al2O3 = 12.39–14.53 wt.%, Fe2O3T = 11.89–13.43 wt.%, CaO = 11.31–14.17 wt.%, MgO = 4.83–5.95 wt.%, Na2O = 1.79–3.08 wt.%, Na2O/K2O = 10–18. In the SiO2 vs. Nb/Y diagram, the samples plot in the gabbro field (fig. 6A). These samples define a typical tholeiitic trend in the SiO2 vs. FeOT/MgO diagram (fig. 6B). The amphibolite samples are depleted in highly incompatible elements and show left-leaning smooth primitive mantle-normalized multi-element patterns, and weakly left-leaning chondrite-normalized REE patterns ((La/Sm)CN= 0.92–1.07, (La/Yb)CN= 1.07–1.20) and negative Eu anomalies (Eu* = 0.62–0.77; fig. 7). The bulk rock samples have εNd(t) = −1.7–+4.5 and εHf(t) = −1.9 (fig. 5B and table 4).

The six metadiorite samples have SiO2 = 59.07–64.56 wt.%, MgO = 2.27–4.12 wt.%, and (K2O + Na2O) = 5.31–7.16 wt.%. In the QAP and An-Ab-Or diagrams, all six samples fall into the granodiorite field. They are weakly peraluminous (A/CNK = 0.84–1.18) and high-K calc-alkaline. The metadiorite samples have strongly negative anomalies of Nb (Nb* = 0.15–0.31), Ta and Sr (Sr* = 0.56–0.73; fig. 7A), and moderately negative to positive Eu anomalies (Eu* = 0.77–1.20) with right-leaning REE patterns (fig. 7B). The metadiorite samples analyzed for their whole-rock Sm-Nd and Lu-Hf isotopes yielded εNd(t) = −0.5–+3.6 and TDM2 age = 2569 – 2910 Ma, εHf(t) = +0.5–+1.4 and TDM2 age = 2916–2968 Ma (fig. 5B and table 4).

DISCUSSION

Neoarchean Basement in the Microcontinents within CAOB

Recently, late Paleoproterozoic (1.8 Ga) rocks were identified in the CAOB (Wang and others, 2006; Pei and others, 2007; Sun and others, 2013), for example, ∼1.8 Ga granites in the borehole of the Songliao Basin (Wang and others, 2006; Pei and others, 2007), ∼1.84 to 1.7 Ga granitic gneisses in the Huma area of the Xing'an Terrane (Sun and others, 2013), ∼1.7 Ga diorite porphyrite and diorite in the central Mongolia Terrane, and ∼1.85 to 1.82 Ga crystalline rocks in the Dzabkhan Terrane in Russia (Kozakov and others, 2007, 2011). Early Mesoproterozoic (1.4 Ga) rocks are also found throughout the CAOB, such as the 1.45 to 1.40 Ga granitoids in the Jiujing region, 1.45 to 1.40 Ga granitoids and amphibolites from the Xingxingxia, Weiya and Alatage areas in the Central Tianshan, 1.46 to 1.43 Ga supracrustal rocks and intrusive rocks in northern Alxa Terrane, ∼1.37 Ga rhyolites at Kyrgyz of North Tianshan, and 1.40 to 1.36 Ga granitoids in Xilinhot Terrane (for example, Kröner and others, 2013; Han and others, 2017; Yuan and others, 2019). In addition, Liu and others (2020) reported one early Neoproterozoic granitic pluton (964–947 Ma) in the Erguna Terrane.

In contrast, confirmed Archean rocks are scarce in the eastern CAOB (Zhou and others, 2018 and references therein). This study has identified the coexistence of Neoarchean amphibolite and metadiorite in the Erguna Terrane (eastern CAOB). Similarly, in the Junggar Terrane (western CAOB), basement enclaves in Ordovician volcanic rocks yielded a Neoarchean magmatic zircon U-Pb age (2522 Ma; Xu and others, 2015). In the central Tianshan Terrane (western CAOB), the protolith age of the orthogneiss has been dated to be 2529 to 2513 Ma by Wang and others (2017). In the central CAOB, a dioritic gneiss yielded magmatic ages of 2546 to 2520 Ma (Kröner and others, 2015). From the detrital zircon age record, Paleozoic sequences

TABLE 3

Major and trace element data of the Biliya amphibolite and metadiorite

Samples	Metadiorite						Amphibolite								
	D18-1-1	D18-1-2	D18-2-1	D18-2-2	D18-7-1	D18-8-1	D18-3-1	D18-3-2	D18-4-1	D18-4-2	D18-4-3	D18-5-1	D18-5-2	D18-6-1	D18-6-2
SiO_2	64.14	64.13	64.56	64.36	59.53	59.07	45.77	44.81	47.12	47.25	46.43	44.96	44.24	51.12	50.79
TiO_2	0.53	0.56	0.52	0.55	1.13	1.17	0.97	1.00	1.11	1.11	1.16	1.09	1.13	0.96	1.00
Al_2O_3	16.31	16.23	14.82	14.53	15.39	15.19	12.78	12.39	14.49	14.53	14.26	14.12	13.84	12.82	12.54
Fe_2O_{3T}	5.91	6.03	6.85	7.11	7.54	7.85	12.74	12.97	13.07	13.09	13.35	13.01	13.43	11.89	12.21
MnO	0.08	0.09	0.13	0.14	0.12	0.13	0.21	0.21	0.19	0.19	0.20	0.20	0.21	0.18	0.18
MgO	2.44	2.59	2.27	2.53	3.88	4.12	5.44	5.69	5.37	5.39	5.73	5.57	5.95	4.83	5.05
CaO	2.40	2.44	3.51	3.71	5.42	5.68	13.60	14.17	11.62	11.61	12.12	12.88	13.45	11.31	11.76
Na_2O	3.62	3.69	3.20	3.26	2.96	2.98	2.15	2.11	2.78	2.77	2.81	2.59	2.58	2.40	2.38
K_2O	3.19	3.48	2.11	2.32	2.49	2.74	0.21	0.21	0.17	0.17	0.16	0.21	0.20	0.16	0.15
P_2O_5	0.17	0.17	0.17	0.17	0.37	0.37	0.08	0.08	0.09	0.09	0.09	0.09	0.08	0.08	0.07
LOI	0.91	1.30	1.50	1.96	0.86	1.49	5.70	6.92	3.60	3.59	4.72	4.84	6.04	3.88	4.96
SUM	99.71	100.19	99.62	100.06	99.69	100.19	99.67	99.48	99.60	99.79	99.84	99.56	99.99	99.62	100.04
Li	31.0	31.2	18.7	17.4	39.9	38.8	14.8	14.0	13.0	12.7	11.8	13.8	12.3	11.7	10.5
Sc	12.3	12.2	15.2	14.5	17.6	17.0	39.6	48.2	44.0	42.6	51.0	45.0	52.9	39.1	46.2
V	82.8	70.8	94.3	81.3	118	107	305	259	349	330	288	338	276	301	256
Cr	71.8	59.7	79.1	75.5	106	89.5	144	173	164	157	184	161	176	140	165
Co	16.3	15.4	19.5	18.0	18.9	23.0	48.3	43.5	52.7	51.0	51.6	52.5	65.5	47.9	44.9
Ni	41.2	36.3	54.0	44.6	26.9	25.8	109	96.3	121	115	104	112	98.0	109	90.8
Ga	20.2	21.0	17.4	18.7	19.7	21.0	15.7	17.5	17.0	16.2	19.4	16.5	18.9	15.1	17.5
Rb	118	121	84.5	86.7	104	106	5.02	6.00	3.50	3.36	5.11	5.52	7.50	3.58	5.67
Sr	382	380	290	285	566	550	117	112	157	151	143	136	134	123	123
Y	15.8	16.7	22.0	21.9	26.3	27.5	22.9	24.6	24.0	23.4	25.3	24.2	25.5	23.3	24.1
Zr	113	110	137	121	262	236	54.4	69.1	60.7	59.5	74.5	58.9	73.7	51.2	62.0
Nb	7.96	8.36	6.22	7.75	18.1	18.8	2.94	3.34	3.04	3.13	2.89	3.12	3.21	2.87	2.76
Cs	6.75	10.2	3.83	5.43	5.91	9.05	0.097	0.22	0.037	0.047	0.10	0.067	0.12	0.043	0.094
Ba	849	936	437	522	786	850	67.0	96.5	68.1	67.2	87.8	61.7	105	57.3	87.7
La	29.1	32.6	24.4	26.8	38.4	43.4	3.68	4.28	3.86	3.54	4.12	3.82	4.11	3.69	4.12
Ce	57.9	63.5	49.9	53.8	82.2	91.5	9.53	10.8	10.3	9.69	10.9	10.0	11.0	9.82	10.5
Pr	6.69	7.52	5.63	6.47	9.57	11.2	1.51	1.74	1.58	1.49	1.78	1.56	1.84	1.46	1.71
Nd	25.9	28.2	21.2	24.1	37.1	41.0	7.46	8.55	7.56	7.85	8.79	8.16	9.16	7.41	8.57
Sm	4.26	4.60	4.12	4.05	6.78	6.92	2.38	2.58	2.48	2.35	2.54	2.57	2.79	2.59	2.48
Eu	1.19	1.43	0.95	1.36	1.89	2.57	0.71	0.71	0.67	0.68	0.64	0.71	0.64	0.59	0.60
Gd	3.61	3.97	3.49	3.65	5.82	6.25	3.28	3.55	3.56	3.41	3.55	3.55	3.57	3.54	3.49
Tb	0.50	0.57	0.54	0.57	0.81	0.87	0.59	0.58	0.61	0.59	0.58	0.64	0.59	0.60	0.55
Dy	2.83	2.90	3.50	3.41	4.64	4.63	3.71	3.84	3.91	3.95	4.07	4.16	4.06	3.87	3.83
Ho	0.54	0.55	0.75	0.71	0.96	0.92	0.85	0.83	0.88	0.85	0.86	0.90	0.86	0.85	0.80
Er	1.51	1.50	2.29	2.02	2.66	2.44	2.40	2.28	2.72	2.43	2.42	2.50	2.37	2.50	2.18
Tm	0.24	0.27	0.36	0.38	0.40	0.45	0.37	0.43	0.43	0.38	0.45	0.42	0.45	0.39	0.42
Yb	1.47	1.68	2.42	2.42	2.48	2.70	2.45	2.62	2.49	2.36	2.76	2.35	2.51	2.20	2.52
Lu	0.24	0.21	0.36	0.34	0.38	0.33	0.36	0.37	0.36	0.37	0.36	0.37	0.37	0.36	0.33
Hf	3.27	3.23	3.81	3.20	6.02	6.29	1.59	1.62	1.82	1.77	1.60	1.78	1.57	1.43	1.49
Ta	0.61	0.65	0.47	0.61	1.15	1.19	0.20	0.20	0.20	0.19	0.23	0.22	0.22	0.19	0.21
Th	7.71	7.27	6.90	6.30	10.5	9.19	0.33	0.39	0.34	0.29	0.38	0.29	0.32	0.26	0.27
U	2.25		2.09		1.91		0.094		0.084	0.071		0.074		0.074	
Mg#	49	50	44	45	55	55	50	51	49	49	50	50	51	49	49
A/CNK	1.18	1.14	1.06	0.99	0.88	0.84	0.45	0.42	0.56	0.56	0.53	0.51	0.48	0.52	0.49
Eu*	0.93	1.02	0.77	1.08	0.92	1.20	0.77	0.72	0.68	0.73	0.65	0.72	0.62	0.60	0.62
Q	24.31	22.22	30.08	27.58	18.71	16.67	5.63	3.79	5.14	5.23	3.02	1.77	0.00	14.60	13.58
Or	20.28	22.01	13.65	15.00	16.15	17.69	1.54	1.52	1.19	1.22	1.12	1.54	1.45	1.12	1.04
Ab	32.99	33.42	29.67	30.10	27.47	27.56	22.42	22.13	28.32	28.25	28.64	26.81	26.69	24.18	23.96
An	11.60	11.78	17.87	18.93	23.36	21.86	30.28	29.42	32.04	32.11	31.17	32.17	31.36	28.31	27.53

$Mg^{\#} = MgO/40.3/(MgO/40.3+FeOt/71.9)$, $A/CNK = Al_2O_3/101.9/(CaO/56.1+Na_2O/62.0+K_2O/94.2)$

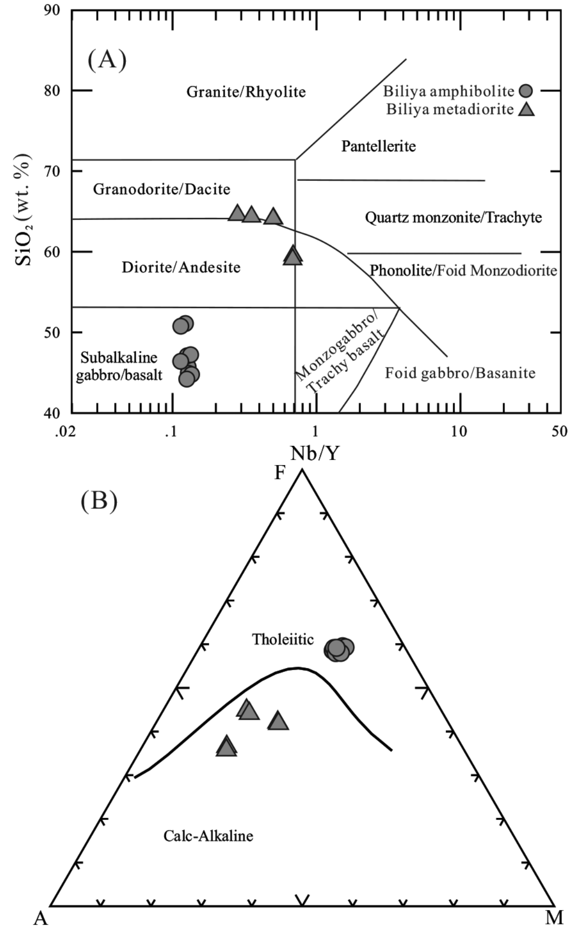

Fig. 6. (A) SiO2-Nb/Y diagram and (C) AFM plot (A=Na2O + K2O; F = FeO+0.8998*Fe2O3; M = MgO).

in the Songliao Terrane (eastern CAOB) yielded a major age peak at 2585 Ma (Zhou and others, 2012). Zhou and others (2018) summarized 390 age data from the Paleozoic sequences in the Kazakhstan–Yili–Central Tianshan Terrane (western CAOB) and identified an age peak at 2510 Ma. In the Beishan Terrane (western CAOB), a slightly younger 2479 Ma age peak was also identified (Zhou and others, 2018). Xu and others (2017) and Liu and others (2020) also reported some detrital zircons with Neoarchean Hf model-ages (2598–2457 Ma). The Paleo-Asian Ocean is widely believed to have closed in late Permian to Triassic (Zhou and Wilde, 2013; Xiao and others, 2015), and these late Archean detrital materials in these terranes with the CAOB were most likely local-sourced. Thus, these Neoarchean igneous and detrital zircons support the contention that Archean basement is present in the micro-continents within the CAOB.

Petrogenesis of the MORB–like Amphibolite: ~20 % Partial Melting of Lithospheric Mantle in the Spinel Stability Field

Though the amphibolite samples show high LOI values (3.59–6.92 wt.%), their chondrite-normalized REE and primitive mantle-normalized multi-element spider

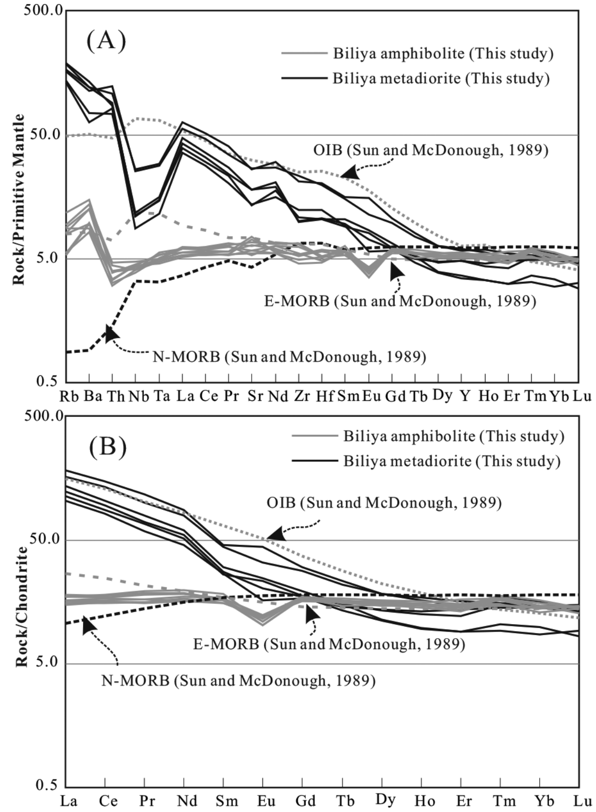

Fig. 7. Primitive mantle-normalized multi-element spidergram (A) and chondrite-normalized REE patterns (B). Normalizing values, and OIB, E-MORB, N-MORB trace elemental contents are from Sun and McDonough (1989).

diagrams exhibit smooth and coherent patterns (fig. 7), suggesting the low mobility of the HFSEs, REEs and Y during post-intrusion metamorphism and alteration. Crustal contamination was likely insignificant, as evidenced by: (1) no inherited zircons, (2) no negative Nb-Ta anomalies, (3) low REE contents and weakly left-leaning REE patterns, (4) low incompatible element contents and left-leaning primitive mantle-normalized multi-element patterns, and (5) lack of Th/Nb vs. La/Sm, Th/Nb vs. εNd(t), or MgO vs. Nb/La correlations. Mantle-derived primary melts commonly have high Ni (>400 ppm) and Cr (>1000 ppm) contents, and Mg# values (73 – 81) (Litvak and Poma, 2010). Our samples show low and variable Mg#, Cr and Ni contents, indicating olivine and clinopyroxene fractionation. Significant negative Eu anomalies (Eu* = 0.62–0.77; fig. 7) also indicate plagioclase fractionation.

Our Neoarchean amphibolite samples are geochemically MORB-like (figs. 7A and 7B). For the trace elemental ratios that are less affected by partial melting (that is good mantle source tracers), our samples are similar to the average primitive mantle (PM; Sun and McDonough, 1989), for example, Th/Nb = 0.11 (PM = 0.12), Hf/Sm = 0.65 (PM = 0.71), Sm/Nd = 0.31 (PM = 0.32), Lu/Hf = 0.22 (PM = 0.24), and Zr/Hf = 38 (PM = 36). In figure 8, all the samples plot close to the PM, also suggesting strong geochemical resemblance with the PM. No correlations exist between the Mg# and these trace elemental ratios, suggesting that these ratios reflect the mantle source features, rather than a fractionation artefact. In figure 8F, the sample Sm/Nd ratios (0.30–0.37, avg. 0.32) plot below the depleted mantle Sm/Nd ratio (0.373) calculated

TABLE 4

Whole-rock Sm-Nd and Lu-Hf isotopic data of the Biliya amphibolite (Samples D18-1-1 and D18-2-1) and metadiorite (Samples D18-3-1, D18-4-1 D18-5-1 and D18-6-1)

Sample	Age (Ga)	$^{147}Sm/^{144}Nd$	$^{143}Nd/^{144}Nd$	$(^{143}Nd/^{144}Nd)_i$	$\varepsilon_{Nd}(t)$	T_{2DM} (Ga)	$^{176}Hf/^{177}Hf$	$^{176}Lu/^{177}Hf$	$(^{176}Hf/^{177}Hf)_i$	ε_{Hf} (t)	T_{2DM} (Ga)
D18-1-1	2.5	0.09963	0.51122	0.50958	3.58	2.6	0.28169	0.01030	0.28119	0.51	2.97
D18-2-1	2.5	0.11757	0.51131	0.50937	-0.54	2.9	0.28187	0.01354	0.28119	1.37	2.92
D18-3-1	2.5	0.19329	0.51277	0.50958	3.67	2.8					
D18-4-1	2.5	0.19826	0.51272	0.50945	1.09	4.2					
D18-5-1	2.5	0.19022	0.51276	0.50963	4.51	2.5					
D18-6-1	2.5	0.21140	0.51279	0.50931	-1.73	5.1	0.28283	0.03562	0.28119	-1.95	3.12

$^{147}Sm/^{144}Nd$ and $^{176}Lu/^{177}Hf$ are calculated using whole-rock Sm-Nd and Lu-Hf contents in table 3. $\varepsilon_{Nd}(t) = (^{143}Nd/^{144}Nd_{sample}/^{143}Nd/^{144}Nd_{CHUR}-1) \times 10000$, $^{143}Nd/^{144}Nd_{CHUR} = 0.512638$. $\varepsilon_{Hf}(t) = (^{176}Hf/^{177}Hf_{sample}/^{176}Hf/^{177}Hf_{CHUR}-1) \times 10000$, $^{176}Hf/^{177}Hf_{CHUR} = 0.282772$. CHUR=Chondrite.

by Salters and Stracke (2004) at 2500 Ma, also supporting that the amphibolite was extracted from a mantle source with PM geochemical characteristics.

The petrogenesis of the amphibolite is dominated by partial melting processes. Ytterbium is compatible in garnet but La and Sm are not, and thus (La/Yb)CN and (Sm/Yb)CN would increase during partial melting in the garnet stability field. Sm and Yb have similar partition coefficients in the partial melting of a spinel lherzolite mantle source, and (Sm/Yb)CN ratios are nearly unfractionated in the melting in the spinel stability field, whereas the Ce/Sm ratios would decrease (Aldanmaz and others, 2000). Our amphibolite samples exhibit flat REEs patterns with low La/Yb)CN (2.0–2.2) and (Sm/Yb)CN (1.4–1.6), and they fall into the spinel lherzolite fields (figs. 9A and B). The calculated average pressure and temperature are 2.0 GPa and 1480 °C (fig. 9C; Till and others, 2012), markedly different from those of present-day Atlantic and Pacific MORB, and correspond to a ~65 km partial melting depth. To determine the degree of partial melting, we conducted petrogenetic modeling with the continuous melting model devised by Zou and Reid (2001). The results suggest that ~20 % melting of the mantle source with PM-like geochemical features in the spinel stability field could best produce the REEs compositions of our amphibolite samples (fig. 9D and table 5), consistent with the results shown in figures 9A and 9B. Thus, we believed that the lithospheric mantle (that is source rocks of the Biliya amphibolites) show PM-like geochemical features and their ~20 % partial melting produced the Biliya amphibolites.

The question remains as how to interpret the whole-rock Nd and Hf isotopic characteristics. The samples yielded wide-ranged εNd(t) (-1.7 to +4.5) and near-zero εHf(t) (-1.9) values, which are significantly lower than those of the present-day Indian, Pacific and Atlantic MORBs formed from the depleted mantle (fig. 5B). Recent Rb-Sr, Sm-Nd, Lu-Hf and Pb-Pb isotopic (Herzberg and others, 2014; Lambart and others, 2019) and seismic anisotropy studies (Bodmer and others, 2015; Moriwaki and others, 2020) have shown that the Earth's mantle is heterogeneous as a result of early planetary differentiation and subsequent crustal recycling during plate tectonics. Thus, though the Neoarchean lithospheric mantle of the Erguna Terrane have PM-like trace elemental features, its Nd-Hf isotopic compositions are heterogeneous and show a wide range of values.

Petrogenesis of the Metadiorite: Partial Melting of Mafic Lower Crust

Our Biliya metadiorites show low SiO2 (59.07–64.56 wt.%) and high Al2O3 (14.53–16.31 wt.%), and variable Eu anomalies (Eu* = 0.77–1.20), suggesting that

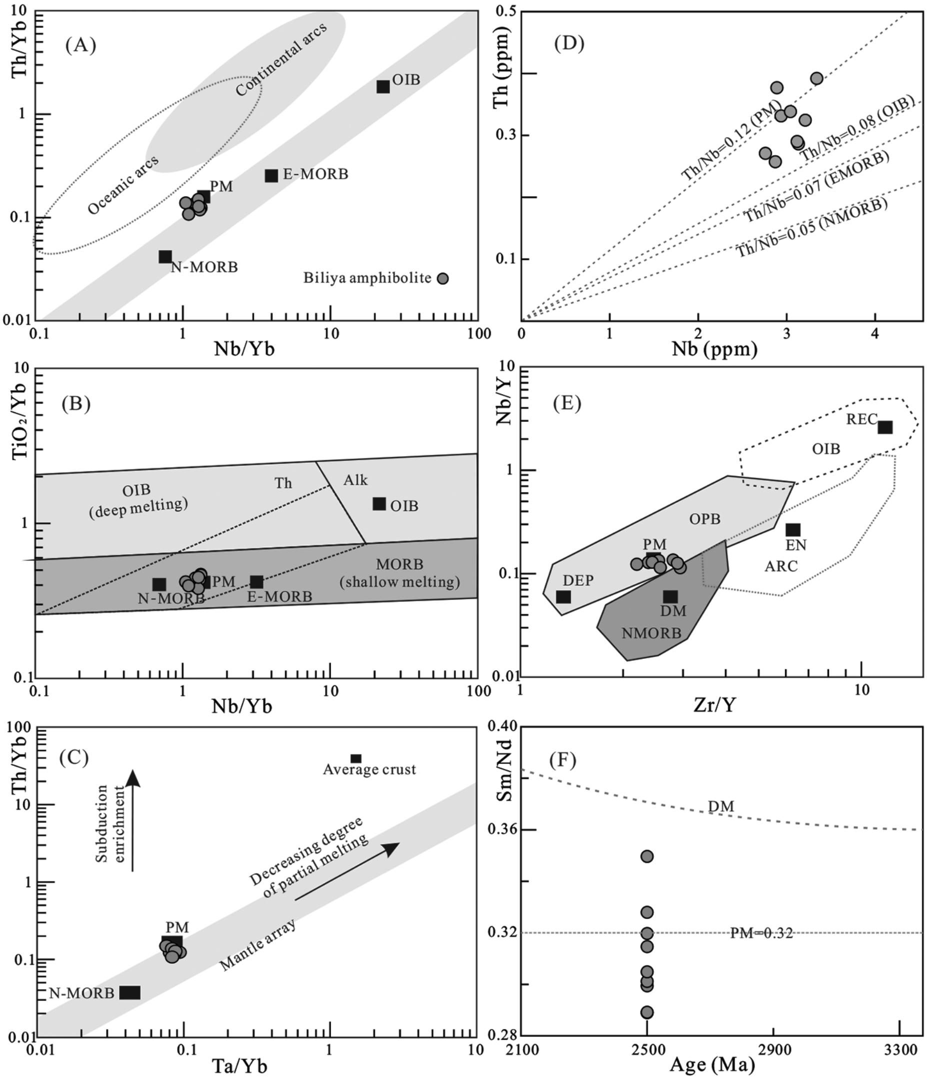

Fig. 8. Binary diagrams of the Biliya amphibolite with the PM. Figures A, B, and C are from Dilek and Furnes (2014) and Furnes and others (2015), and figures D, E, and F are from Cook and others (2016). Abbrevations: E-MORB – enriched mid-ocean ridge basalt, BABB – back-arc basin basalt, FAB – forearc basalt, IAT – island arc tholeiite, PM – primitive mantle, DM – depleted mantle.

fractional crystallization did not play an important role in their petrogenesis. The metadiorites show low FeOT/MgO and A/CNK ratios (0.84−1.18) ratios, Zr and Zr + Nb + Ce + Y contents, high whole-rock εNd(t) (−0.5 – +3.6) and εHf(t) (+0.5 – +1.4) values. They contain no high-temperature anhydrous minerals, but some hornblendes. The Biliya metadiorites are I-type granitoids. I-type granite is generally derived from dehydration melting of igneous rock or their metamorphic equivalents (Chappell and others 1998; Chappell 1999). The low A/CNK ratios (0.84−1.18) precludes their derivation from melting of a sedimentary source or melting of an igneous source under water-saturated condition because both processes would produce strongly peraluminous melts (Douce and Johnston, 1991; Douce, 1996). The low SiO2 contents (59.07–64.56 wt.%) for our Biliya metadiorite samples suggest a mafic

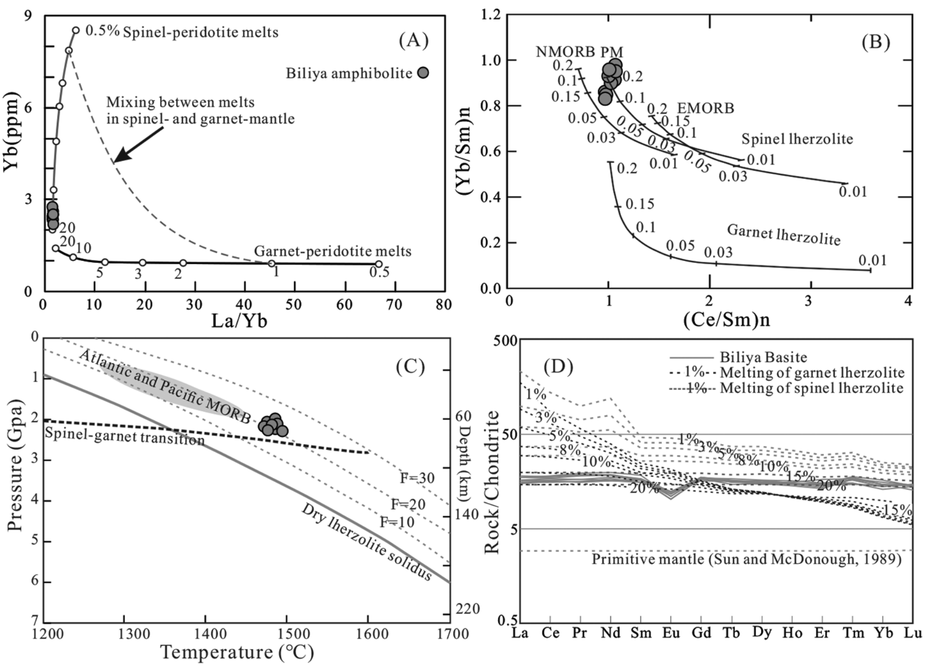

Fig. 9. (A) Yb vs. La/Yb plot (Tschegg and others, 2011), (B) (Yb/Sm)n vs. (Ce/Sm)n plot (Cook and others, 2016), (C) Pressure-temperature diagram showing the temperature and melting depth of the Biliya amphibolite (Cook and others, 2016; Till and others, 2012), (D) REE modeling results for continuous mantle melting of the PM in the spinel and garnet stability fields. The modeling parameters and data are shown in table 5.

source, such as amphibolite. Experimental studies have demonstrated that partial melting of basaltic rocks can produce intermediate to silicic melts leaving a granulite residue at 8 to 12 kbar or an eclogite residue at 12 to 32 kbar (Rapp and Watson, 1995). Thus, it is likely that our Biliya metadiorites are originated from partial melting of sub-alkaline meta-basalts (that is amphibolite).

Based on the absence or presence respectively of initially inherited zircons, the I-type granites were classified into two distinct types, high- and low-temperature (Chappell and others, 1998). No inherited zircons have been found in our Biliya metadiorite samples. We carried out whole rock zirconium saturation temperature (TZr) calculation and got the TZr in a range of 796 to 852 °C, and thus the Biliya metadiorites are high-temperature I-type granitoids. The high-temperature I-type granites formed from a magma that was completely or largely molten (Chappell and others, 1998). Previous experiments reveal that water-unsaturated dehydration melting of the meta-basalts can generate mildly peraluminous melt with high K content (Rapp and Watson 1995; Chappell and others, 2012), and water-saturated melting of the meta-basalts yield strong peraluminous melts (Beard and Lofgren 1991). The Biliya metadiorites are weakly peraluminous (A/CNK = 0.84–1.18), and they should be generated by water-unsaturated dehydration melting of the meta-basalts. The meta-basalts constituted the ancient mafic lower crust of the region.

Experimental data has demonstrated that biotite and muscovite will breakdown when the temperature is higher than 800 to 850 °C (Thompson and Connolly 1995), but dehydration melting of amphibolites requires much higher temperatures (>1000 °C, Rapp and Watson, 1995). Residual mineral assembles after melt extraction may also play a crucial role in forming magmas with peculiar geochemical characteristics

TABLE 5
Trace element modeling results

	Spinel lherzolite partial melting							Garnet lherzolite partial melting						
No.	1	2	3	4	5	6	7	1	2	3	4	5	6	7
F	0.01	0.03	0.05	0.08	0.10	0.15	0.20	0.01	0.03	0.05	0.08	0.10	0.15	0.20
Th	9.14	2.93	1.73	1.07	0.86	0.57	0.43	8.68	2.93	1.73	1.07	0.86	0.57	0.43
Nb	66.19	24.50	14.54	9.02	7.19	4.78	3.58	58.86	24.28	14.53	9.02	7.19	4.78	3.58
Ta	3.81	1.41	0.84	0.52	0.41	0.27	0.21	3.38	1.40	0.84	0.52	0.41	0.27	0.21
La	53.87	23.27	14.00	8.69	6.93	4.61	3.45	40.99	21.80	13.83	8.68	6.93	4.61	3.45
Ce	83.41	51.56	34.83	22.37	17.90	11.90	8.91	52.23	39.04	29.98	21.28	17.52	11.88	8.91
Pr	9.19	6.66	4.97	3.41	2.77	1.85	1.39	5.34	4.46	3.75	2.94	2.53	1.81	1.38
Nd	54.78	36.46	25.73	16.96	13.63	9.08	6.80	18.18	16.18	14.42	12.18	10.92	8.42	6.65
Zr	168.11	149.08	132.08	110.11	97.62	72.99	56.11	103.99	96.68	89.85	80.46	74.74	62.21	51.96
Hf	4.64	4.11	3.64	3.04	2.69	2.01	1.55	2.87	2.67	2.48	2.22	2.06	1.72	1.43
Sm	6.94	6.12	5.40	4.47	3.94	2.91	2.23	3.72	3.51	3.30	3.00	2.82	2.40	2.03
Eu	2.60	2.30	2.04	1.69	1.49	1.11	0.84	1.21	1.16	1.11	1.03	0.98	0.86	0.75
Ti	11782	10996	10248	9195	8541	7066	5824	7220	6975	6733	6373	6137	5556	4994
Gd	8.59	7.70	6.88	5.80	5.17	3.89	2.99	3.27	3.21	3.14	3.03	2.96	2.76	2.55
Tb	1.36	1.24	1.13	0.98	0.89	0.69	0.54	0.49	0.49	0.48	0.47	0.47	0.45	0.44
Dy	9.19	8.41	7.67	6.66	6.05	4.72	3.69	3.09	3.08	3.06	3.04	3.03	2.99	2.94
Y	39.05	36.98	34.95	32.02	30.14	25.71	21.69	8.89	9.15	9.45	9.98	10.41	11.90	15.39
Ho	1.88	1.74	1.60	1.41	1.29	1.03	0.82	0.60	0.60	0.61	0.61	0.61	0.62	0.63
Er	4.89	4.56	4.25	3.81	3.53	2.90	2.36	1.59	1.60	1.62	1.64	1.65	1.70	1.78
Tm	0.80	0.74	0.69	0.61	0.56	0.45	0.37	0.21	0.22	0.22	0.23	0.23	0.25	0.27
Yb	4.23	4.01	3.79	3.47	3.27	2.79	2.35	1.12	1.15	1.18	1.23	1.27	1.41	1.66
Lu	0.60	0.57	0.54	0.50	0.47	0.40	0.35	0.14	0.14	0.15	0.15	0.16	0.18	0.23

(Beard and Lofgren, 1991). The flat HREE patterns and their TZr (796−852 °C) may suggest amphibole as residual mineral and biotite and muscovite melting. Significant Sr (Sr* = 0.56–0.73), and variable Eu anomalies (Eu* = 0.77–1.20) imply that plagioclase might also play as residual mineral in the magma chamber (Martin, 1999). Thus, the Biliya metadiorites were generated by dehydration melting of biotite/muscovite from sub-alkaline meta-basalts, leaving amphibole and plagioclase as the major residual minerals.

Neoarchean Mantle Enrichment and Crustal Extraction in Continental Arc/back–arc Setting

Generation of MORB-type rocks is generally linked to local/regional extension: 1) mantle wedge plume activity (Castro and others, 2010); 2) mid-ocean ridge seafloor spreading (Ridley and others, 2009; Yang and others, 2018); 3) post-orogenic lithospheric delamination (Priestley and others, 2012); and 4) slab rollback-induced back-arc extension (MacLeod and others, 2013). Mantle wedge plume activity is often associated with widespread OIB-type mafic magmatism, and no Neoarchean OIB-type rocks have been found in the Erguna Terrane. Rocks in mid-ocean ridge seafloor spreading show highly depleted Nd and Hf isotopic compositions, with highly positive εHf(t) and εNd(t) values (fig. 5B; Kempton and others, 2002). No evidence for major Neoarchean lithospheric delamination has been found in the microcontinents within the CAOB. Thus, the first three scenarios are considered unlikely. In figure 10, our amphibolite samples fall into the back-arc basin basalt (BABB) field or between the volcanic arc basalt (VAB) and MORB fields, and they were thus likely to have formed in a back-arc basin setting. In this setting (fig. 11B), hot asthenosphere upwelling close to the Moho may have provided sufficient heat for the partial melting of lithospheric mantle in the spinel stability field (~65 km). I-type granites can be generated in various continental tectonic settings, rather than intra-oceanic settings (Roberts

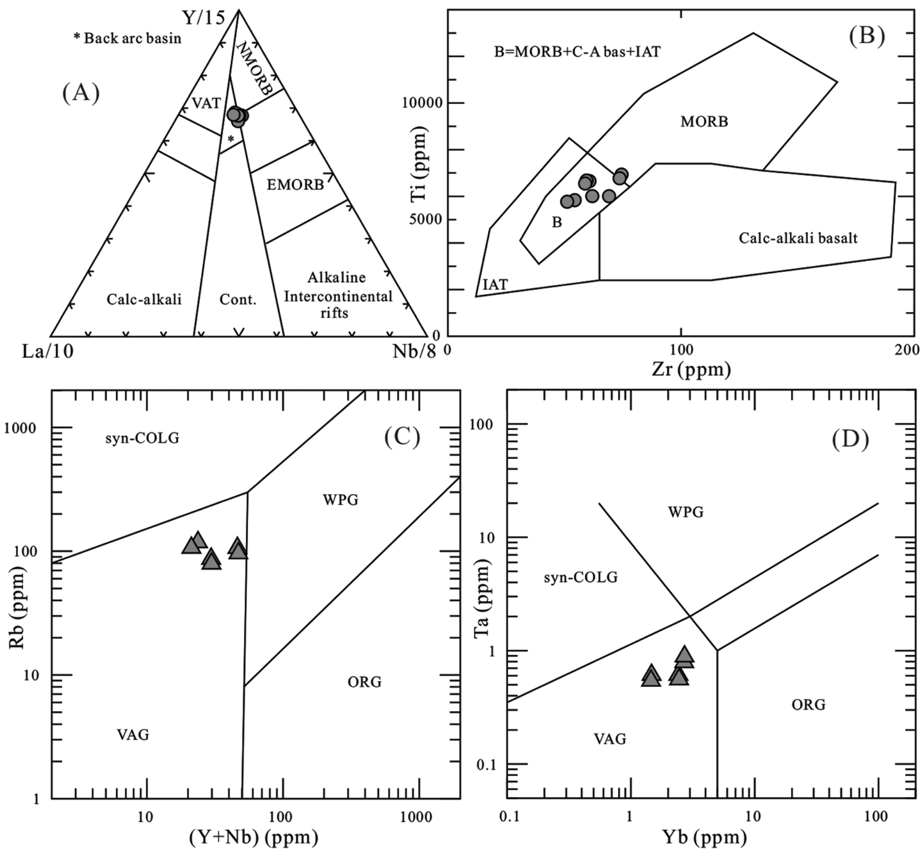

Fig. 10. Tectonic discrimination diagrams of the Biliya amphibolite (A and B) and granodiorite (C and D). Abbrevations: VAT – Volcanic arc tholeiite, E-MORB – enriched mid-oceanic-ridge basalt, N-MORB – normal mid-oceanic- ridge basalt, IAT – island-arc tholeiite, VAG – volcanic arc granites, ORG – ocean ridge granites, WPG – within-plate granites, SYN-COLG – syn-collisional granites.

and Clemens 1993). In the tectonic discrimination diagrams, the Biliya metadiorites fall into the volcanic-arc granite field (fig. 10). Considering their coexistence, the Biliya amphibolites and metadiorites are likley formed in a continental arc/back-arc setting.

In comparison with present-day Indian, Pacific, and Atlantic MORBs formed from the depleted mantle, our MORB-like amphibolites have enriched Nd-Hf isotopic compositions with a relatively wide range of values εNd(t) = −1.7 to +4.5 and εHf(t) = −1.9 (fig. 5B). These εNd(t)-εHf(t) values suggest that the Neoarchean lithospheric mantle (that is source of the Biliya amphibolites) has been significantly enriched. Thus, an enriched mantle and TTG crust have been identified in this study. From the lithospheric mantle to the TTG crust, three-stage mantle segregation may have happened: (1) PM-like lithospheric mantle melting: 20 % melt extraction from lithospheric mantle left a depleted mantle and produced the Biliya MORB-type amphibolite (fig. 11B); (2) Mantle enrichment: metasomatism of PM-like lithospheric mantle by subduction-related fluids and/or melts, and substantial arc-type enriched mantle and mafic lower crust were generated (figs. 11A and 11C); and, (3) Lower crust melting: large-scale partial melting of the mafic lower crust produced the TTG crust (fig. 11C), that is crustal extraction.

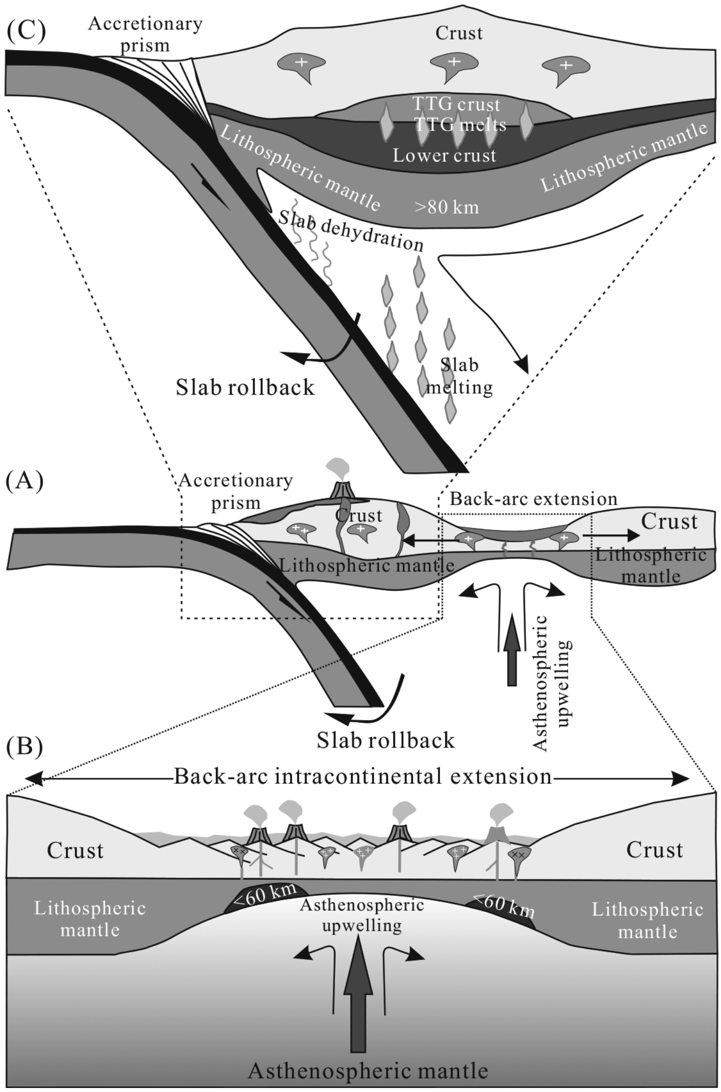

Fig. 11. Schematic tectonic diagram showing the three-staged mantle segregation and the generations of the PUM, arc-type enriched mantle, and TTG crust.

CONCLUSIONS

(1) Neoarchean amphibolite and metadiorite are identified in the Erguna Terrane. The former is derived from ~20 % partial melting of the lithospheric mantle in the spinel stability field (~65 km), and the latter is generated by the partial melting of mafic lower crust.

(2) The Biliya amphibolite and metadiorite were formed in arc/back-arc extension setting, and their identification confirms the presence of Neoarchean basement in the microcontinents within the CAOB.

(3) Three-staged mantle segregation processes have been proposed: (a) 20 % melt extraction from PM-like lithospheric mantle, leaving behind a depleted mantle; (b) subduction-related fluid/melt metasomatism of the PM-like lithospheric mantle

and its partial melting, generating the arc-type enriched mantle and mafic lower crust; (c) partial remelting of the mafic lower crust produced the TTG crust.

ACKNOWLEDGMENTS

The study was funded by the Science Foundation of China University of Petroleum (Beijing) (No. 2462018YJRC030 and 2462020YXZZ020) and National Natural Science Foundation of China (No. 42072150). We are grateful to Associate Editor Peter A. Cawood and two anonymous reviewers for their constructive and helpful reviews. We declare that we have no financial and personal relationships with other people or organizations that can inappropriately influence our work, there is no professional or other personal interest of any nature or kind in any product, service and/or company that could be construed as influencing the position presented in, or the review of, the manuscript entitled.

REFERENCES

Albarède, F., Blichert-Toft, J., Vervoort, J. D., Gleason, J. D., and Rosing, M., 2000, Hf–Nd isotope evidence for a transient dynamic regime in the early terrestrial mantle: Nature, v. 404, p. 488–490, https://doi.org/10.1038/35006621

Aldanmaz, E., Pearce, J. A., Thirlwall, M. F., and Mitchell, J. G., 2000, Petrogenetic evolution of late Cenozoic, post-collision volcanism in western Anatolia, Turkey: Journal of Volcanology and Geothermal Research, v. 102, n. 1–2, p. 67–95, https://doi.org/10.1016/S0377-0273(00)00182-7

Anderson, D. L., 1983, Chemical composition of the mantle: Journal of Geophysical Research: Solid Earth, v. 88, n. S01, p. B41, https://doi.org/10.1029/JB088iS01p00B41

Beard, J. S., and Lofgren, G. E., 1991, Dehydration Melting and Water-Saturated Melting of Basaltic and Andesitic Greenstones and Amphibolites at 1, 3, and 6. 9 kb: Journal of Petrology, v. 32, n. 2, p. 365–401, https://doi.org/10.1093/petrology/32.2.365

Bodmer, M., Toomey, D. R., Hooft, E. E., Nábělek, J., and Braunmiller, J., 2015, Seismic anisotropy beneath the Juan de Fuca plate system: Evidence for heterogeneous mantle flow: Geology, v. 43, n. 12, p. 1095–1098, https://doi.org/10.1130/G37181.1

Castro, A., Gerya, T., García-Casco, A., Fernandez, C., Díaz-Alvarado, J., Moreno-Ventas, I., and Löw, I., 2010, Melting Relations of MORB-Sediment Mélanges in Underplated Mantle Wedge Plumes; Implications for the Origin of Cordilleran-type Batholiths: Journal of Petrology, v. 51, n. 6, p. 1267–1295, https://doi.org/10.1093/petrology/egq019

Cawood, P. A., Hawkesworth, C. J., and Dhuime, B., 2013, The continental record and the generation of continental crust: Geological Society of America Bulletin, v. 125, n. 1–2, p. 14–32, https://doi.org/10.1130/B30722.1

Cawood, P. A., and Hawkesworth, C. J., 2019, Continental crustal volume, thickness and area, and their geodynamic implications: Gondwana Research, v. 66, p. 116–125, https://doi.org/10.1016/j.gr.2018.11.001

Chappell, B. W., 1999, Aluminium saturation in I- and S-type granites and the characterization of fractionated haplogranites: Lithos, v. 46, n. 3, p. 535–551, https://doi.org/10.1016/S0024-4937(98)00086-3

Chappell, B. W., Bryant, C. J., and Wyborn, D., 2012, Peraluminous I-type granites: Lithos, v. 153, p. 142–153, https://doi.org/10.1016/j.lithos.2012.07.008

Chappell, B. W., Bryant, C. J., Wyborn, D., White, A. J. R., and Williams, I. S., 1998, High- and Low-Temperature I-type Granites: Resource Geology, v. 48, n. 4, p. 225–235, https://doi.org/10.1111/j.1751-3928.1998.tb00020.x

Compston, W., Williams, I. S., and Meyer, C., 1984, U-Pb geochronology of zircons from lunar breccia 73217 using a sensitive high mass-resolution ion microprobe: Journal of Geophysical Research: Solid Earth, v. 89, n. S02, p. B525–B534, https://doi.org/10.1029/JB089iS02p0B525

Cook, Y. A., Sanislav, I. V., Hammerli, J., Blenkinsop, T. G., and Dirks, P. H. G. M., 2016, A primitive mantle source for the Neoarchean mafic rocks from the Tanzania Craton: Geoscience Frontiers, v. 7, n. 6, p. 911–926, https://doi.org/10.1016/j.gsf.2015.11.008

Cui, F., Zheng, C., Xu, X., Yao, W., Ding, X., Shi, L., and Li, J., 2015, Detrital zircon ages of the Jiageda and Woduhe formations: Constrains on the tectonic attribute of the Xing' an terrane in the central Great Xing' an Range, NE China: Journal of Asian Earth Sciences, v. 113, Part 1, p. 427–442, https://doi.org/10.1016/j.jseaes.2015.01.017

Dilek, Y., and Furnes, H., 2014, Ophiolites and Their Origins: Elements, v. 10, n. 2, p. 93–100, https://doi.org/10.2113/gselements.10.2.93

Douce, A. E. P., 1996, Effects of pressure and H2O content on the compositions of primary crustal melts: Earth and Environmental Science Transactions of the Royal Society of Edinburgh, v. 87, n. 1–2, p. 11–21, https://doi.org/10.1017/S026359330000643X

Douce, A. E. P., and Johnston, A. D., 1991, Phase equilibria and melt productivity in the pelitic system: implications for the origin of peraluminous granitoids and aluminous granulites: Contributions to Mineralogy and Petrology, v. 107, p. 202–218, https://doi.org/10.1007/BF00310707

Eizenhöfer, P. R., Zhao, G. C., Zhang, J., Han, Y. G., Hou, W. Z., Liu, D. X., and Wang, B., 2015, Geochemical characteristics of the Permian basins and their provenances across the Solonker Suture Zone: Assessment of net crustal growth during the closure of the Palaeo-Asian Ocean: Lithos, v. 224–225, p. 240–255, https://doi.org/10.1016/j.lithos.2015.03.012

Furnes, H., Dilek, Y., and de Wit, M., 2015, Precambrian greenstone sequences represent different ophiolite types: Gondwana Research, v. 27, n. 2, p. 649–685, https://doi.org/10.1016/j.gr.2013.06.004

Gou, J., Sun, D. Y., Ren, Y. S., Liu, Y. J., Zhang, S. Y., Fu, C. L., Wang, T. H., Wu, P. F., and Liu, X. M., 2013, Petrogenesis and geodynamic setting of Neoproterozoic and Late Paleozoic magmatism in the Manzhouli-Erguna area of Inner Mongolia, China: Geochronological, geochemical and Hf isotopic evidence: Journal of Asian Earth Sciences, v. 67–68, p. 114–137, https://doi.org/10.1016/j.jseaes.2013.02.016

Han, J., Zhou, J.-B., Li, L., and Song, M.-C., 2017, Mesoproterozoic (~1.4 Ga) A-type gneissic granites in the Xilinhot terrane, NE China: First evidence for the break-up of Columbia in the eastern CAOB: Precambrian Research, v. 296, p. 20–38, https://doi.org/10.1016/j.precamres.2017.04.043

Hanchar, J. M., and Miller, C. F., 1993, Zircon zonation patterns as revealed by cathodoluminescence and backscattered electron images: Implications for interpretation of complex crustal histories: Chemical Geology, v. 110, n. 1–3, p. 1–13, https://doi.org/10.1016/0009-2541(93)90244-D

Hawkesworth, C. J., and Kemp, A. I. S., 2006, Evolution of the continental crust: Nature, v. 443, p. 811–817, https://doi.org/10.1038/nature05191

Hawkesworth, C. J., Dhuime, B., Pietranik, A. B., Cawood, P. A., Kemp, A. I. S., and Storey, C. D., 2010, The generation and evolution of the continental crust: Journal of the Geological Society, v. 167, p. 229–248, https://doi.org/10.1144/0016-76492009-072

Herzberg, C., Cabral, R. A., Jackson, M. G., Vidito, C., Day, J. M. D., and Hauri, E. H., 2014, Phantom Archean crust in Mangaia hotspot lavas and the meaning of heterogeneous mantle: Earth and Planetary Science Letters, v. 396, p. 97–106, https://doi.org/10.1016/j.epsl.2014.03.065

Hofmann, A. W., 1988, Chemical differentiation of the Earth: the relationship between mantle, continental crust, and oceanic crust: Earth and Planetary Science Letters, v. 90, n. 3, p. 297–314, https://doi.org/10.1016/0012-821X(88)90132-X

IMBGMR (Inner Mongolian Bureau of Geology Mineral Resources), 1991, Regional Geology of Inner Mongolia: Geological Publishing House, Beijing, p. 1–725 (in Chinese).

Jian, P., Kröner, A., and Zhou, G., 2012, SHRIMP zircon U–Pb ages and REE partition for high-grade metamorphic rocks in the North Dabie complex: Insight into crustal evolution with respect to Triassic UHP metamorphism in east-central China: Chemical Geology, v. 328, p. 49–69, https://doi.org/10.1016/j.chemgeo.2012.01.015

Kemp, A. I. S., Hawkesworth, C. J., Collins, W. J., Gray, C. M., and Blevin, P. L., 2009, Isotopic evidence for rapid continental growth in an extensional accretionary orogen: The Tasmanides, eastern Australia: Earth and Planetary Science Letters, v. 284, n. 3–4, p. 455–466, https://doi.org/10.1016/j.epsl.2009.05.011

Kempton, P. D., Pearce, J. A., Barry, T. L., Fitton, J. G., Langmuir, C., and Christie, D. M., 2002, Sr-Nd-Pb-Hf Isotope Results from ODP Leg 187: Evidence for Mantle Dynamics of the Australian-Antarctic Discordance and Origin of the Indian MORB Source: Geochemistry, Geophysics, Geosystems, v. 3, n. 12, p. 1–35, https://doi.org/10.1029/2002GC000320

Kovach, V. P., Kozakov, I. K., Salnikova, E. B., Yarmolyuk, V. V., Kozlovsky, A. M., and Terent'eva, L. B., 2013, Crustal growth stages in the Songino block of the early caledonian superterrane in Central Asia: II. Geochemical and Nd-isotope data: Petrology, v. 21, p. 409–426, https://doi.org/10.1134/S0869591113050020

Kozakov, I. K., Kozlovsky, A. M., Yarmolyuk, V. V., Kovach, V. P., Bibikova, E. V., Kirnozova, T. I., Plotkina, Y. V., Zagornaya, N. Y., Fugzan, M. M., Erdenejargal, C., Lebedev, V. I., and Eenjin, G., 2011, Crystalline complexes of the Tarbagatai block of the Early Caledonian superterrane of Central Asia: Petrology, v. 19, p. 426–444, https://doi.org/10.1134/S0869591111040047

Kozakov, I. K., Sal'nikova, E. B., Wang, T., Didenko, A. N., Plotkina, Y. V., and Podkovyrov, V. N., 2007, Early Precambrian crystalline complexes of the Central Asian microcontinent: Age, sources, tectonic position: Stratigraphy and Geological Correlation, v. 15, p. 121–140, https://doi.org/10.1134/S0869593807020013

Kröner, A., Alexeiev, D. V., Rojas-Agramonte, Y., Hegner, E., Wong, J., Xia, X., Belousova, E., Mikolaichuk, A. V., Seltmann, R., Liu, D., and Kiselev, V. V., 2013, Mesoproterozoic (Grenville-age) terranes in the Kyrgyz North Tianshan: Zircon ages and Nd–Hf isotopic constraints on the origin and evolution of basement blocks in the southern Central Asian Orogen: Gondwana Research, v. 23, n. 1, p. 272–295, https://doi.org/10.1016/j.gr.2012.05.004

Kröner, A., Kovach, V. P., Kozakov, I. K., Kirnozova, T., Azimov, P., Wong, J., and Geng, H. Y., 2015, Zircon ages and Nd–Hf isotopes in UHT granulites of the Ider Complex: A cratonic terrane within the Central Asian Orogenic Belt in NW Mongolia: Gondwana Research, v. 27, n. 4, p. 1392–1406, https://doi.org/10.1016/j.gr.2014.03.005

Lambart, S., Koornneef, J. M., Millet, M.-A., Davies, G. R., Cook, M., and Lissenberg, C. J., 2019, Highly heterogeneous depleted mantle recorded in the lower oceanic crust: Nature Geoscience, v. 12, p. 482–486, https://doi.org/10.1038/s41561-019-0368-9

Li, X., Li, Z.-X., Zhou, H., Liu, Y., and Kinny, P. D., 2002, U–Pb zircon geochronology, geochemistry and Nd isotopic study of Neoproterozoic bimodal volcanic rocks in the Kangdian Rift of South China: implications for the initial rifting of Rodinia: Precambrian Research, v. 113, n. 1–2, p. 135–154, https://doi.org/10.1016/S0301-9268(01)00207-8

Litvak, V. D., and Poma, S., 2010, Geochemistry of mafic Paleocene volcanic rocks in the Valle del Cura region: Implications for the petrogenesis of primary mantle-derived melts over the Pampean flat-slab:

Journal of South American Earth Sciences, v. 29, n. 3, p. 705–716, https://doi.org/10.1016/j.jsames.2010.01.001

Liu, H., Li, Y., Wan, Z., and Lai, C.-K., 2020, Early Neoproterozoic tectonic evolution of the Erguna Terrane (NE China) and its paleogeographic location in Rodinia supercontinent: Insights from magmatic and sedimentary record: Gondwana Research, v. 88, p. 185–200, https://doi.org/10.1016/j.gr.2020.07.005

Liu, Y., Gao, S., Hu, Z., Gao, C., Zong, K., and Wang, D., 2010, Continental and Oceanic Crust Recycling-induced Melt-Peridotite Interactions in the Trans-North China Orogen: U-Pb Dating, Hf Isotopes and Trace Elements in Zircons from Mantle Xenoliths: Journal of Petrology, v. 51, n. 1–2, p. 537–571, https://doi.org/10.1093/petrology/egp082

Ludwig, K. R., 2001, Sqiud 1.02: A User Manual: Berkeley, California, Berkeley Geochronological Center Special Publication, 219 p.

Luan, J.-P., Yu, J.-J., Yu, J.-L., Cui, Y.-C., and Xu, W.-L., 2019, Early Neoproterozoic magmatism and the associated metamorphism in the Songnen Massif, NE China: Petrogenesis and tectonic implications: Precambrian Research, v. 328, p. 250–268, https://doi.org/10.1016/j.precamres.2019.04.004

MacLeod, C. J., Johan Lissenberg, C., and Bibby, L. E., 2013, "Moist MORB" axial magmatism in the Oman ophiolite: The evidence against a mid-ocean ridge origin: Geology, v. 41, n. 4, p. 459–462, https://doi.org/10.1130/G33904.1

Martin, H., 1999, Adakitic magmas: modern analogues of Archaean granitoids: Lithos, v. 46, n. 3, p. 411–429, https://doi.org/10.1016/S0024-4937(98)00076-0

Miao, L., Liu, D., Zhang, F., Fan, W., Shi, Y., and Xie, H., 2007, Zircon SHRIMP U-Pb ages of the "Xinghuadukou Group" in Hanjiayuanzi and Xinlin areas and the "Zhalantun Group" in Inner Mongolia, Da Hinggan Mountains: Chinese Science Bulletin, v. 52, p. 1112–1124, https://doi.org/10.1007/s11434-007-0131-2

Ming, Z., Sun, J. G., Yan, J., Zhao, S. F., Zhu, J. Q., Liu, C., Feng, Y. Y., and Yang, M., 2015, Forming environment and magmatic-hydrothermal evolution history of andesite in Deerbuer lead-zinc deposit of eastern Inner Mongolia: Zircon U–Pb dating: Global Geology, v. 34, n. 3, p. 590–598 (in Chinese with English abstract).

Moriwaki, R., Usui, T., Tobita, M., and Yokoyama, T., 2020, Geochemically heterogeneous Martian mantle inferred from Pb isotope systematics of depleted shergottites: Geochimica et Cosmochimica Acta, v. 274, p. 157–171, https://doi.org/10.1016/j.gca.2020.01.014

Pei, F., Xu, W., Yang, D., Zhao, Q., Liu, X., and Hu, Z., 2007, Zircon U-Pb geochronology of basement metamorphic rocks in the Songliao Basin: Chinese Science Bulletin, v. 52, p. 942–948, https://doi.org/10.1007/s11434-007-0107-2

Priestley, K., McKenzie, D., Barron, J., Tatar, M., and Debayle, E., 2012, The Zagros core: Deformation of the continental lithospheric mantle: Geochemistry, Geophysics, Geosystems, v. 13, n. 11, p. Q11014, https://doi.org/10.1029/2012GC004435

Rapp, R. P., and Watson, E. B., 1995, Dehydration Melting of Metabasalt at 8-32 kbar: Implications for Continental Growth and Crust-Mantle Recycling: Journal of Petrology, v. 36, n. 4, p. 891–931, https://doi.org/10.1093/petrology/36.4.891

Ridley, W. I., Perfit, M. R., and Wanless, D., 2009, Evolution of MORB at fast-spreading ridges: Goldschmidt Abstracts 2009–R, Geochimica et Cosmochimica Acta, v. 73, n. 13, Supplement, p. A1100, https://doi.org/10.1016/j.gca.2009.05.014

Roberts, M. P., and Clemens, J. D., 1993, Origin of high-potassium, talc-alkaline, I-type granitoids: Geology, v. 21, n. 9, p. 825–828, https://doi.org/10.1130/0091-7613(1993)021<0825:OOHPTA>2.3.CO;2

Salters, V. J. M., and Stracke, A., 2004, Composition of the depleted mantle: Geochemistry, Geophysics, Geosystems, v. 5, n. 5, p. Q05B07, https://doi.org/10.1029/2003GC000597

Sun, L. X., Ren, B. F., Zhao, F. Q., Ji, S. P., and Geng, J. Z., 2013, Late Paleoproterozoic magmatic records in the Eerguna massif: evidences from the zircon U-Pb dating of granitic gneisses: Geology Bulletin of China, v. 32, p. 41–352 (in Chinese with English abstract).

Sun, S. -S., and McDonough, W. F., 1989, Chemical and isotopic systematics of oceanic basalts: implications for mantle composition and processes: Geological Society, London, Special Publications, v. 42, n. 1, p. 313–345, https://doi.org/10.1144/GSL.SP.1989.042.01.19

Sun, W., Chi, X.-G., Zhao, Z., Pan, S.-Y., Liu, J.-F., Zhang, R., and Quan, J.-Y., 2014, Zircon geochronology constraints on the age and nature of 'Precambrian metamorphic rocks' in the Xing'an block of Northeast China: International Geology Review, v. 56, n. 6, p. 672–694, https://doi.org/10.1080/00206814.2014.883183

Tang, G., Wang, Q., Wyman, D. A., Li, Z.-X., Zhao, Z.-H., Jia, X.-H., and Jiang, Z.-Q., 2010, Ridge subduction and crustal growth in the Central Asian Orogenic Belt: Evidence from Late Carboniferous adakites and high-Mg diorites in the western Junggar region, northern Xinjiang (west China): Chemical Geology, v. 277, n. 3–4, p. 281–300, https://doi.org/10.1016/j.chemgeo.2010.08.012

Thompson, A. B., and Connolly, J. A. D., 1995, Melting of the continental crust: Some thermal and petrological constraints on anatexis in continental collision zones and other tectonic settings: Journal of Geophysical Research: Solid Earth, v. 100, n. B8, p. 15565–15579, https://doi.org/10.1029/95JB00191

Till, C. B., Grove, T. L., and Krawczynski, M. J., 2012, A melting model for variably depleted and enriched lherzolite in the plagioclase and spinel stability fields: Journal of Geophysical Research: Solid Earth, v. 117, p. B06206, https://doi.org/10.1029/2011JB009044

Tschegg, C., Ntaflos, T., and Akinin, V. V., 2011, Polybaric petrogenesis of Neogene alkaline magmas in an extensional tectonic environment: Viliga Volcanic Field, northeast Russia: Lithos, v. 122, n. 1–2, p. 13–24, https://doi.org/10.1016/j.lithos.2010.11.009

van Hunen, J., and Moyen, J.-F., 2012, Archean Subduction: Fact or Fiction? Annual Review of Earth and Planetary Sciences, v. 40, p. 195–219, https://doi.org/10.1146/annurev-earth-042711-105255

Vervoort, J. D., Patchett, P. J., Albarède, F., Blichert-Toft, J., Rudnick, R., and Downes, H., 2000, Hf–Nd isotopic evolution of the lower crust: Earth and Planetary Science Letters, v. 181, n. 1–2, p. 115–129, https://doi.org/10.1016/S0012-821X(00)00170-9

Wang, X.-S., Gao, J., Klemd, R., Jiang, T., Li, J.-L., Zhang, X., and Xue, S.-C., 2017, The Central Tianshan Block: A microcontinent with a Neoarchean-Paleoproterozoic basement in the southwestern Central Asian Orogenic Belt: Precambrian Research, v. 295, p. 130–150, https://doi.org/10.1016/j.precamres.2017.03.030

Wang, Y., Zhang, F., Zhang, D., Miao, L., Li, T., Xie, H., Meng, Q., and Liu, D., 2006, Zircon SHRIMP U-Pb dating of meta-diorite from the basement of the Songliao Basin and its geological significance: Chinese Science Bulletin, v. 51, p. 1877–1883, https://doi.org/10.1007/s11434-006-2035-y

White, W. M., 1985, Sources of oceanic basalts: Radiogenic isotopic evidence: Geology, v. 13, n. 2, p. 115–118, https://doi.org/10.1130/0091-7613(1985)13<115:SOOBRI>2.0.CO;2

Wilde, S. A., and Zhou, J.-B., 2015, The late Paleozoic to Mesozoic evolution of the eastern margin of the Central Asian Orogenic Belt in China: Journal of Asian Earth Sciences, v. 113, p. 909–921, https://doi.org/10.1016/j.jseaes.2015.05.005

Wu, F.-Y., Sun, D.-Y., Ge, W.-C., Zhang, Y.-B., Grant, M. L., Wilde, S. A., and Jahn, B.-M., 2011, Geochronology of the Phanerozoic granitoids in northeastern China: Journal of Asian Earth Sciences, v. 41, n. 1, p. 1–30, https://doi.org/10.1016/j.jseaes.2010.11.014

Wu, F.-Y., Yang, Y.-H., Xie, L.-W., Yang, J.-H., and Xu, P., 2006, Hf isotopic compositions of the standard zircons and baddeleyites used in U–Pb geochronology: Chemical Geology, v. 234, n. 1–2, p. 105–126, https://doi.org/10.1016/j.chemgeo.2006.05.003

Wu, G., Chen, Y., Chen, Y., and Zeng, Q., 2012, Zircon U–Pb ages of the metamorphic supracrustal rocks of the Xinghuadukou Group and granitic complexes in the Argun massif of the northern Great Hinggan Range, NE China, and their tectonic implications: Journal of Asian Earth Sciences, v. 49, p. 214–233, https://doi.org/10.1016/j.jseaes.2011.11.023

Xiao, W., Windley, B. F., Sun, S., Li, J., Huang, B., Han, C., Yuan, C., Sun, M., and Chen, H., 2015, A Tale of Amalgamation of Three Permo-Triassic Collage Systems in Central Asia: Oroclines, Sutures, and Terminal Accretion: Annual Review of Earth and Planetary Sciences, v. 43, p. 477–507, https://doi.org/10.1146/annurev-earth-060614-105254

Xie, H. Q., Mang, F. Q., Miao, L. C., Chen, F. K., and Liu, D. Y., 2008, Zircon SHRIMP U-Pb dating of the amphibolite from "Heilongjiang Group" and the granite in Mudanjiang area, NE China, and its geological significance: Acta Petrologica Sinica, v. 24, n. 6, p. 1237–1250 (in Chinese with English abstract).

Xu, B., Zhao, G., Li, J., Liu, D., Wang, B., Han, Y., Eizenhöfer, P. R., Zhang, X., Hou, W., and Liu, Q., 2017, Ages and Hf isotopes of detrital zircons from Paleozoic strata in the Chagan Obo Temple area, Inner Mongolia: Implications for the evolution of the Central Asian Orogenic Belt: Gondwana Research, v. 43, p. 149–163, https://doi.org/10.1016/j.gr.2016.08.004

Xu, M., Xu, W., Wang, F., and Gao, F., 2012, Age, association and provenance of the "Neoproterozoic" fengshuigouhe group in the northwestern Lesser Xing'an Range, NE China: Constraints from zircon U-Pb geochronology: Journal of Earth Science, v. 23, p. 786–801, https://doi.org/10.1007/s12583-012-0291-0

Xu, X.-W., Li, X.-H., Jiang, N., Li, Q.-L., Qu, X., Yang, Y.-H., Zhou, G., and Dong, L.-H., 2015, Basement nature and origin of the Junggar terrane: New zircon U–Pb–Hf isotope evidence from Paleozoic rocks and their enclaves: Gondwana Research, v. 28, n. 1, p. 288–310, https://doi.org/10.1016/j.gr.2014.03.011

Yang, S., Humayun, M., and Salters, V. J. M., 2018, Elemental Systematics in MORB Glasses From the Mid-Atlantic Ridge: Geochemistry, Geophysics, Geosystems, v. 19, m. 11, p. 4236–4259, https://doi.org/10.1029/2018GC007593

Yang, Y. H., Zhang, H. F., Wu, F. Y., Xie, L. W., and Zhang, Y. B., 2005, Accurate measurement of strontium isotopic composition by neptune multiple collector inductively coupled plasma mass spectrometry: Journal of Chinese Mass Spectrometry Society, v. 26, p. 215–221 (in Chinese with English abstract).

Yang, H., Ge, W., Zhao, G., Bi, J., Wang, Z., Dong, Y., and Xu, W., 2017, Zircon U–Pb ages and geochemistry of newly discovered Neoproterozoic orthogneisses in the Mishan region, NE China: Constraints on the high-grade metamorphism and tectonic affinity of the Jiamusi–Khanka Block: Lithos, v. 268–271, p. 16–31, https://doi.org/10.1016/j.lithos.2016.10.017

Yang, J.-H., Wu, F.-Y., Wilde, S. A., Belousova, E., and Griffin, W. L., 2008, Mesozoic decratonization of the North China block: Geology, v. 36, n. 6, p. 467–470, https://doi.org/10.1130/G24518A.1

Yang, J.-H., Wu, F.-Y., Shao, J.-A., Wilde, S. A., Xie, L., and Liu, X.-M., 2006, Constraints on the timing of uplift of the Yanshan Fold and Thrust Belt, North China: Earth and Planetary Science Letters, v. 246, n. 3–4, p. 336–352, https://doi.org/10.1016/j.epsl.2006.04.029

Yuan, Y., Zong, K., Cawood, P. A., Cheng, H., Yu, Y., Guo, J., Liu, Y., Hu, Z., Zhang, W., and Li, M., 2019, Implication of Mesoproterozoic (~1.4 Ga) magmatism within microcontinents along the southern Central Asian Orogenic Belt: Precambrian Research, v. 327, p. 314–326, https://doi.org/10.1016/j.precamres.2019.03.014

Zhang, Y.-H., Xu, W.-L., Tang, J., Wang, F., Xu, M.-J., and Wang, W., 2014, Age and provenance of the Ergunahe Group and the Wubinaobao Formation, northeastern Inner Mongolia, NE China: implications for tectonic setting of the Erguna Massif: International Geology Review, v. 56, n. 6, p. 653–671, https://doi.org/10.1080/00206814.2013.877856

Zhao, S., Xu, W.-L., Tang, J., Li, Y., and Guo, P., 2016, Timing of formation and tectonic nature of the purportedly Neoproterozoic Jiageda Formation of the Erguna Massif, NE China: Constraints from field geology and U–Pb geochronology of detrital and magmatic zircons: Precambrian Research, v. 281, p. 585–601, https://doi.org/10.1016/j.precamres.2016.06.014

Zhao, Y., Lv, J., Zhang, D., Zhou, Y., Shao, J., and Wang, B., 2017, Rb- Sr isochron age of De'rbur Pb - Zn - Ag deposit in Erguna Terrane of northeast Inner Mongolia and its geological significance: Mineral Deposits, v. 36, n. 4, p. 893–904 (in Chinese with English abstract).

Zhao, Y., Lv, J., Zhang, P., Zhang, D., Shen, X., and Bi, Z., 2018, Characteristics of Ore-Forming Fluids in the De'rbur Pb-Zn-Ag Deposit in the NW Great Hinggan Mountains and its Significance: Acta Geologica Sinica, v. 92, n. 1, p. 142–153 (in Chinese with English abstract).

Zhou, J.-B., and Wilde, S. A., 2013, The crustal accretion history and tectonic evolution of the NE China segment of the Central Asian Orogenic Belt: Gondwana Research, v. 23, n. 4, p. 1365–1377, https://doi.org/10.1016/j.gr.2012.05.012

Zhou, J.-B., Wilde, S. A., Zhao, G.-C., and Han, J., 2018, Nature and assembly of microcontinental blocks within the Paleo-Asian Ocean: Earth-Science Reviews, v. 186, p. 76–93, https://doi.org/10.1016/j.earscirev.2017.01.012

Zhou, J.-B., Wilde, S. A., Zhang, X.-Z., Liu, F.-L., and Liu, J.-H., 2012, Detrital zircons from phanerozoic rocks of the Songliao Block, NE China: Evidence and tectonic implications: Journal of Asian Earth Sciences, v. 47, p. 21–34, https://doi.org/10.1016/j.jseaes.2011.05.004

Zhou, J.-B., Cao, J.-L., Wilde, S. A., Zhao, G.-C., Zhang, J.-J., and Wang, B., 2014, Paleo-Pacific subduction-accretion: Evidence from Geochemical and U-Pb zircon dating of the Nadanhada accretionary complex, NE China: Tectonics, v. 33, n. 12, p. 2444–2466, https://doi.org/10.1002/2014TC003637

Zindler, A., Jagoutz, E., and Goldstein, S., 1982, Nd, Sr and Pb isotopic systematics in a three-component mantle: a new perspective: Nature, v. 298, p. 519–523, https://doi.org/10.1038/298519a0

Zou, H., and Reid, M. R., 2001, Quantitative modeling of trace element fractionation during incongruent dynamic melting: Geochimica et Cosmochimica Acta, v. 65, n. 1, p. 153–162, https://doi.org/10.1016/S0016-7037(00)00505-6

Zong, K., Klemd, R., Yuan, Y., He, Z., Guo, J., Shi, X., Liu, Y., Hu, Z., and Zhang, Z., 2017, The assembly of Rodinia: The correlation of early Neoproterozoic (*ca.* 900 Ma) high-grade metamorphism and continental arc formation in the southern Beishan Orogen, southern Central Asian Orogenic Belt (CAOB): Precambrian Research, v. 290, p. 32–48, https://doi.org/10.1016/j.precamres.2016.12.010